MOTION COMPENSATION OF INTERFEROMETRIC SYNTHETIC APERTURE RADAR

by

David P. Duncan

A thesis submitted to the faculty of

Brigham Young University

in partial fulfillment of the requirements for the degree of

Master of Science

Department of Electrical and Computer Engineering

Brigham Young University

August 2004

BRIGHAM YOUNG UNIVERSITY

GRADUATE COMMITTEE APPROVAL

of a thesis submitted by

David P. Duncan

This thesis has been read by each member of the following graduate committee and by majority vote has been found to be satisfactory.

Date	David G. Long, Chair
Date	Karl F. Warnick
Date	Randal W. Beard

BRIGHAM YOUNG UNIVERSITY

As chair of the candidate's graduate committee, I have read the thesis of David P. Duncan in its final form and have found that (1) its format, citations, and bibliographical style are consistent and acceptable and fulfill university and department style requirements; (2) its illustrative materials including figures, tables, and charts are in place; and (3) the final manuscript is satisfactory to the graduate committee and is ready for submission to the university library.

Date

David G. Long
Chair, Graduate Committee

Accepted for the Department

Michael A. Jensen
Graduate Coordinator

Accepted for the College

Douglas M. Chabries
Dean, College of Engineering and Technology

ABSTRACT

MOTION COMPENSATION OF INTERFEROMETRIC SYNTHETIC APERTURE RADAR

David P. Duncan

Department of Electrical and Computer Engineering

Master of Science

Deviations from a nominal, straight-line flight path of a synthetic aperture radar (SAR) lead to inaccurate and defocused radar images. This thesis is an investigation into the improvement of the motion compensation algorithm created for the BYU inteferometric synthetic aperture radar, YINSAR. The existing BYU SAR processing algorithm produces improved radar imagery but does not fully account for variations in attitude (roll, pitch, yaw) and does not function well with large position deviations. Results in this thesis demonstrate that a higher order motion compensation algorithm is not as effective as using a segmented reference track, coupled with the current lower-order motion compensation algorithm. Attitude variations cause a Doppler shift and are corrected by limiting the processed azimuth bandwidth or by reversing the frequency shift with a range-dependent filter. Another important area considered is the effects of motion compensation on interferometry. When performing interferometry with YINSAR, motion compensating both channels to a single track has two effects. First, the applied MOCO phase corrections remove the "flat-earth"

differential phase from the interferogram. Second, range resampling coregisters the two images. All of these changes have helped to improve YINSAR imagery.

ACKNOWLEDGMENTS

I would first like to thank Dr. David Long for his constant support, guidance and aid throughout the research process. He saw and helped me see my potential all aLong the way. I also want to thank my wife, Julie, and my family for their love and continual support. Finally, and most importantly, I want to thank God for having given me the opportunity to study at this University and for the opportunity to deal with this research.

Contents

List of Tables

List of Figures

Chapter 1

Introduction

Synthetic aperture radar (SAR) is a valuable remote sensing tool in many arenas. Its applications vary from environmental monitoring to military surveillance. As technology improves, so does the cost and reliability of SAR. In 1995, Brigham Young University created a low-cost, interferometric SAR using off-the-shelf hardware and custom programming. This low-cost SAR, called YINSAR, helps to demonstrate the feasibility of a high-resolution radar imaging system at minimal financial cost.

One of the primary assumptions made during SAR processing is that the radar carrying vehicle, or platform, moves along a straight-line path with a constant velocity. However, this ideal imaging situation is rarely present due to piloting errors, wind gusts, and other complications. To prevent image degradation, these motion errors must be compensated. Basic motion compensation (MOCO) consists of three principle steps: measuring the aircraft motion using motion sensors (accelerometers, gyros and GPS), calculating a reference straight-line path, and calculating and applying motion corrections. These steps are dependent upon the imaging parameters of the radar system. When the radar has an azimuth beamwidth that is small, motion compensation is simplified. However, when the azimuth beamwidth is large, motion compensation becomes much more complicated.

In 1999, Richard Lundgreen created a motion compensation algorithm for YINSAR which consisted of phase correction, range resampling, and azimuth resampling [1]. While this motion compensation algorithm improves some YINSAR imagery, it does not perform well with longer collections. This suboptimal performance on these important cases motivates improvement of the motion compensation algorithm.

An important step to improved YINSAR imagery is the development of a SAR signal model and the implementation of better SAR processing algorithms. The most common SAR processing algorithm is the range-Doppler algorithm which makes many approximations to simplify SAR processing. Other newer processing algorithms such as the Chirp-Scaling and the Wavenumber Domain algorithms were implemented to improve the achievable resolution and computation time.

Different levels of motion motivate varying degrees of motion compensation. The chosen motion compensation algorithm depends upon the size of the azimuth beamwidth as well as the magnitude of the position deviations from the selected reference track. When a small azimuth beamwidth is present with small deviations, a simple motion compensation known as a narrowbeam or first-order motion correction, can be used. However, with a large azimuth beamwidth or large deviations, more complex, higher order motion corrections are required. Such algorithms often require more computational time.

The existing YINSAR motion compensation algorithm can be improved by including Doppler centroid estimation and correction techniques, by considering higher order motion compensation, and by using a segmented reference track. Attitude errors (roll, pitch, yaw) in a radar carrying vehicle create antenna pointing problems. These problems result in a Doppler shift of the received data, known as a Doppler centroid variation. If left unresolved, these Doppler shifts can cause unwanted image artifacts. Doppler centroid variations are corrected either by limiting azimuth processing bandwidth or by shifting the data back to zero Doppler. The next area of improvement is the development of higher order motion compensation algorithms with application to YINSAR. Large deviations caused by a single reference track over long flights with high platform motion require a higher order motion compensation algorithms. Two such motion compensation algorithms exist that employ higher order motion corrections. Both algorithms proceed by applying a first-order or narrowbeam correction, and then applying a higher order correction. Although both algorithms initially appeared promising, they often produce degraded YINSAR imagery. Instead I adopt a final improvement by segmenting the reference track. With this technique,

a reference track is created for each image segment, lowering the track deviations significantly during image formation. Although this method can increase computational time due to increased overlap, it also has the distinct advantage of being able to use the current YINSAR motion compensation algorithm.

This thesis analyzes these motion compensation techniques and advanced processing as applied to YINSAR. The results indicate that using a segmented reference track with first-order motion compensation results in improved YINSAR imagery more than with higher order motion compensation algorithms. Also, Doppler centroid variations are minimized through increasing the processed azimuth bandwidth. Finally, a theoretical evaluation of the motion compensation of an interferometric system with two bistatic channels produces similar results to systems with only one bistatic channel.

The thesis is organized as follows:

- **Chapter 2** covers basic radar imaging and SAR theory, various SAR processing algorithms, interferometry theory, and provides background on Brigham Young University's interferometric SAR, YINSAR.

- **Chapter 3** delves into the modeling of motion in the SAR data model, considers its effects on final images, and discusses three motion compensation algorithms to correct various types of motion errors.

- **Chapter 4** discusses the application of motion compensation techniques to YINSAR and discusses how MOCO relates to interferometry of a dual bistatic radar.

- **Chapter 5** summarizes the results and discusses the future work relating to YINSAR.

Chapter 2

Background

Synthetic aperture radar (SAR) has become a very important modern remote sensing tool and has found a variety of applications in military, topographical, and environmental situations. This background chapter is designed to provide a basic understanding of SAR imaging theory, and various SAR processing algorithms.

2.1 SAR History

Radar has been a valuable tool throughout much of the 20th century in tracking aircraft and ships. It was not until the late 1930s that engineers began to attach the radar antenna to the fuselage of aircraft. This idea led to the beginning of side-looking aperture radars (SLARs) in the field of radar imaging. For SLAR, the best imaging resolution is dependent upon the size of the antenna. In June of 1951 Carl Wiley described the use of Doppler frequency analysis to improve radar image resolution. The technique was originally called Doppler beam sharpening, but today is known as synthetic aperture radar [6].

2.2 SAR Geometry

The basic SAR geometry model and its variables can be seen in Fig. 2.1 and is used throughout this thesis. The radar carrying vehicle, or platform, is located at $(x, 0, -h)$ and moves along a straight line trajectory, or track, at a constant velocity, V. As shown in the model, the range, R, from the platform to a target located at $(x', y', 0)$ is a three dimensional range function and is given by

$$R(x', x, y', h) = \sqrt{(x' - x)^2 + (y')^2 + (h)^2}. \tag{2.1}$$

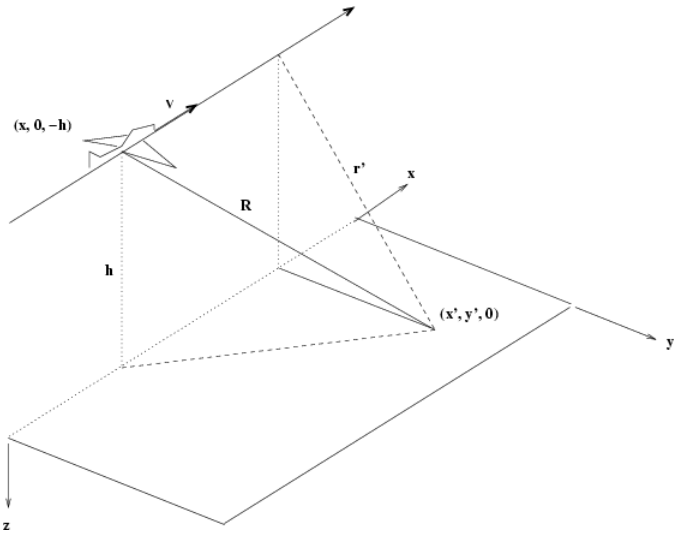

Figure 2.1: SAR imaging geometry

This distance of the radar to its target area is called the slant range or cross-track direction while the platform flight trajectory is known as the azimuth or along-track direction. The path along the ground to the target area known as the ground range. A common convention in many texts is to refer to the slant range as simply the range direction.

The coordinate system shown consists of right-handed coordinate axes, with the positive x axis in the azimuth direction, negative z axis representing the platform height above the ground, and positive y pointing along the ground range direction. When dealing with radar images, this three dimensional geometry can be reduced to two dimensions. This is done by substituting the near-range function

$$r' = \sqrt{(y')^2 + (h)^2} \tag{2.2}$$

into Eq. (2.1) which reduces the range-to-target function to

$$R(r', x', x) = \sqrt{(r')^2 + (x' - x)^2}. \tag{2.3}$$

This reduction helps to simplify the inversion problem and is used in many SAR processing algorithms.

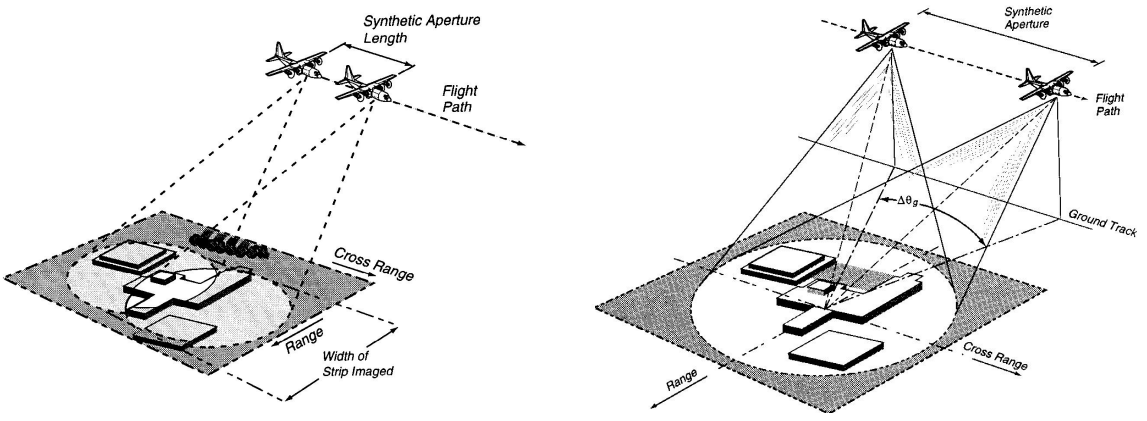

(a) (b)

Figure 2.2: (a) Stripmap and (b) Spotlight imaging geometries [2]

Another important factor in the SAR geometry model is the azimuth angle of the antenna beam, or squint angle. This angle may or may not be controlled by the radar operator and defines how the beam is steered. A beam constantly steered (either mechanically or electronically) toward the target area is known as spotlight SAR imaging. However, if the squint angle is held constant during a flight over the target area, the resulting image is an image "strip" parallel with the flight track. This type of data collection is known as stripmap SAR. Most stripmap SAR typically operate with a squint angle orthogonal to the direction of travel, or in a broadside direction. These imaging methods are illustrated in Fig. 2.2.

The frequency at which the radar transmits pulses is known as the pulse repetition frequency, or PRF. As is discussed in [7], the PRF determines the ambiguity in the range and azimuth directions.

2.3 Range Resolution

Range resolution is a defining parameter of a radar and represents the minimum distance targets can be separated and be distinguished by the radar. The two main factors affecting range resolution are the transmit pulse shape and the pulse length. This section discusses two pulses: the interrupted continuous wave (ICW) and the linear frequency modulated (LFM) chirp. The latter half of the section explains the techniques of matched filtering or range compression to improve range resolution.

2.3.1 ICW

An ICW pulse of amplitude a and pulse length T_p is given by

$$p(t) = \begin{cases} a & : \quad 0 < t < T_p \\ 0 & : \quad t < 0;\, t > T_p. \end{cases} \tag{2.4}$$

In a hypothetical situation, if a transmitted ICW pulse reflects off two targets located at different ranges, they can be resolved by the radar if the trailing edge of the closer target's echo arrives to the radar before the forward edge of the further target's echo. The resolvable distance is then directly dependent upon the length of the square pulse, T_p, with the resolution given by

$$\Delta R = \frac{c\Delta t}{2} = \frac{cT_p}{2}. \tag{2.5}$$

So to improve the resolution, a shorter pulse is needed. Unfortunately, while shortening the pulse improves range resolution, it also decreases the received signal to noise ratio. This tradeoff between SNR and resolution makes the ICW pulse an undesirable choice.

2.3.2 LFM Chirp

As previously noted, a decrease in a square pulse's length improves range resolution, but is also accompanied by a decrease in the signal to noise ratio. A common solution to the tradeoff is to use a modulation or phase encoding scheme

on the transmitted pulse. Any modulation scheme can be used, but one of the most widely implemented is the linear-frequency modulated (LFM) chirp because of its ease of implementation. This modulation is a sinusoid which linearly increases in frequency with time (see Fig. 2.3) and is properly named a chirp, for when heard in an audible frequency range it resembles the chirp of a bird. The LFM chirp is defined as

$$p(t) = \exp\left(j\pi\beta t^2\right) \tag{2.6}$$

where β is known as the chirp rate. The chirp can either be modulated up (known as an up chirp) or down (a down chirp) in frequency. One of the most important characteristics of this waveform is its correlation property, that is, when a chirp is correlated with itself, a *sinc* function is the result (Fig. 2.3). This correlated waveform contains the same energy as the original modulated waveform; however, the energy is concentrated around the time bin corresponding to the delay. This correlation property is often referred to as matched filtering or range compression.

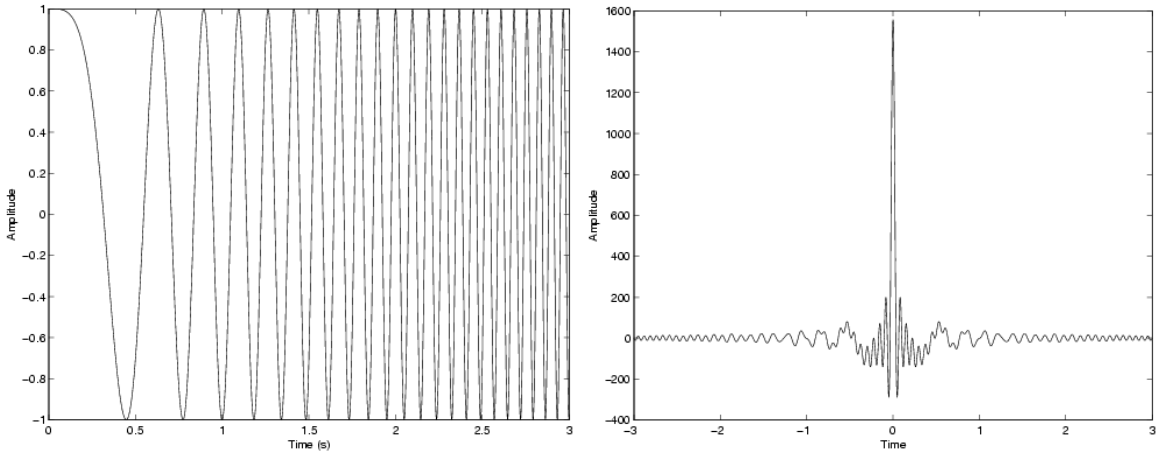

(a) (b)

Figure 2.3: An (a) uncompressed and (b) compressed LFM chirp

2.3.3 Range Matched filtering

An important technique in the improvement of range resolution is matched filtering or pulse compression. The matched filter is a tool used in radar and communications to produce the maximum achievable signal SNR when the signal plus additive white noise are received. As explained in [1], the fundamental factor in determining achievable radar range resolution is the bandwidth of the transmitted pulse.

Following the derivation in [6] and [1], the SNR at the output of a matched filter (SNR_{out}) is related to the SNR at the matched filter's input (SNR_{in}) by

$$SNR_{out} = \tau_p B_n SNR_{in} \tag{2.7}$$

where τ_p is the transmit pulse length and B_n transmitted signal bandwidth. The value of $\tau_p B_n$ is known as the time bandwidth product and represents the gain achieved through using a matched filter. Therefore, both transmit pulse length and pulse bandwidth effect radar range resolution. The ideal matched filter is mathematically represented by the correlation of the transmitted pulse, $p(t)$, with the received,

$$s(t) = \int p(\tau) p^*(\tau + t)\, d\tau. \tag{2.8}$$

This operation of matched filtering is typically performed in the frequency domain where the correlation operation becomes a multiplication. While any pulse modulation can be used, one of the commonly used pulses with high matched filter SNR is the LFM chirp.

2.4 Azimuth Resolution

While improved range resolution is achievable through matched filtering, good radar imagery also requires high azimuth resolution. Two important methods of radar imaging are real and synthetic aperture radar imaging. The azimuth resolution of real aperture radar imaging is dependent upon the azimuth beamwidth of the transmitting antenna while synthetic aperture resolution is inversely proportional to the size of the azimuth beamwidth.

2.4.1 Real Aperture Radar

In a real aperture radar system the azimuth resolution is dependent upon the azimuth beamwidth. The azimuth resolution of a real aperture can be derived from the imaging geometry and is given by [4]

$$\delta_{az} = 2r' \tan\left(\frac{\theta_a}{2}\right) \tag{2.9}$$

where θ_a is the azimuth angle, and r' is the near range. Using the approximations $\theta_a \approx \lambda/L_{az}$ and $\delta_{az} \approx r'\theta_a$, the azimuth resolution is

$$\delta_{az} \approx \frac{r'\lambda}{L_{az}} \tag{2.10}$$

where λ is the carrier wavelength, and L_{az} is the azimuth antenna length. Taking into account the height of the platform

$$h = r' \cos(\theta_i) \tag{2.11}$$

where θ_i is the radar look angle, the real aperture azimuth resolution becomes

$$\delta_{az} \approx \frac{h\lambda}{\cos(\theta_i) L_{az}}. \tag{2.12}$$

This result shows that the constraining factors on real aperture radar azimuth resolution are the maximum size of the antenna carried by the platform and the platform height.

2.4.2 Synthetic Aperture Radar

Synthetic aperture radar was described by Wiley as "Doppler beam-forming" [6]. As a radar flies over a target transmitting pulses, each of the echoes from the target have a different frequency shift due to the velocity of the platform. Observing the frequency shift from the target over many pulses closely resembles that of an LFM chirp, which suggests matched filtering in the azimuth dimension. While using the Doppler effect to explain SAR is useful to understanding the concept, in actuality the observed frequency shift over the pulses has nothing to do directly with the velocity of the aircraft. The shift is actually a result of observing the changing target phase.

As the radar moves along the track from one pulse collection to the next, each pulse collected has a phase dependent upon the range to the target. Piecing together various pulses collected from different points along the flight track forms what is known as a phase history of the target. Thus, the synthetic aperture is better viewed as a phased array antenna, where each pulse represents an element and the spacing of the elements is dictated by the radar PRF and its velocity. The only part the platform velocity plays in the imaging is to move the radar from one position to the next. Matched filtering of this phase history improves azimuth resolution and effectively narrows the azimuth beamwidth.

An approximation of the azimuth resolution for synthetic aperture radar can be estimated using the idea of a synthetic array antenna. As shown in [4], a radar with an azimuth antenna of length L_{az} moving at a constant velocity, the length of the synthetic array is equivalent to size of the beam footprint on the ground. The size of the synthetic array given as

$$L_s = \frac{2\lambda h}{L_{az}} \tag{2.13}$$

where L_{az} is the azimuth size of the antenna and h is the height of the platform. The new $3dB$ azimuth beamwidth of the synthesized array is

$$\theta_{SAR} \approx \frac{\lambda}{L_s} = \frac{L_s}{2h}. \tag{2.14}$$

The corresponding azimuth synthesized resolution is given by

$$\delta_{SAR} \approx h\theta_{SAR} = \frac{L_s}{2} \tag{2.15}$$

This result demonstrates two important points about SAR: first, to improve the azimuth resolution of a radar image, the physical antenna length must be decreased. Second, the azimuth resolution is independent of changes in platform height. While these results seem contradictory, they are better explained by observing the larger antenna footprint on the ground they cause. In the first case, as the azimuth antenna size is decreased, the azimuth ground footprint increases, which allows for more observations of the target and consequently creates a longer target phase history which

improves azimuth resolution. Similarly, an increase in the platform height also increases the length of target phase histories and improves azimuth resolution. While synthetic aperture radar provides a large improvement in azimuth resolution over real aperture radar, it requires coherent radar hardware to preserve signal phase, larger amounts of data storage, and increased amounts of processing. The next section develops the SAR signal model and discusses various processing algorithms used in the SAR community.

2.5 SAR Processing

As has been shown, synthetic aperture radar has better resolution than real aperture radar; however, the trade off for increased resolution is signal processing complexity. The key to understanding SAR processing and motion compensation is understanding the SAR data model. The SAR processing or azimuth compression algorithms discussed here include Range-Doppler, Wavenumber Domain, and Chirp Scaling algorithms [8].

2.5.1 SAR Signal Model

Derivations of the SAR signal model can be found in [6], [8], [9], and [10]. The particular approach to the model taken here follows the treatment by Bamler [8]. To begin the derivation of this signal model, the transmitted radar pulse is written

$$p_{transmitted}(t) = p(t) \exp j\omega_0 t \tag{2.16}$$

where $p(t)$ is the transmitted pulse and ω_0 is the carrier frequency. After reception and demodulation of the echo from a scatterer located at a distance (r', x'), the received set of pulses at the radar location $x = vt$ is given by

$$d(x,t) = \sigma p(t - 2R(r', x', x)/c) \exp\left[-j\omega_0 2R(r', x', x)/c\right] \tag{2.17}$$

where $R(r', x', x)$ is given by the hyperbolic range-to-target function (Eq. (2.3)) and σ is the target reflectivity. Assuming an ideal range matched filter, the range compressed form of $p(t)$ becomes a $\text{sinc}(\cdot)$. However, for simplicity in this case, it is assumed to

be $\delta(\cdot)$. Thus, the range compressed collection of pulses from the target is represented as

$$d(x,t) = \sigma\delta(t - \frac{2}{c}R(r',x',x)) \exp\left[-j\omega_0 \frac{2}{c}R(r',x',x)\right]. \tag{2.18}$$

Equation (2.18) is known as the SAR point spread response (PSR) and gives insight into the nature of the SAR signal and its processing. This function can be visualized by an approximate LFM chirp in the azimuth direction (formed from the phase function $\exp(\cdot)$) that is bent along the azimuth "smiles" formed from the $\delta(\cdot)$ function (Fig. 2.4). The two-dimensional coupling of the range and azimuth in the target

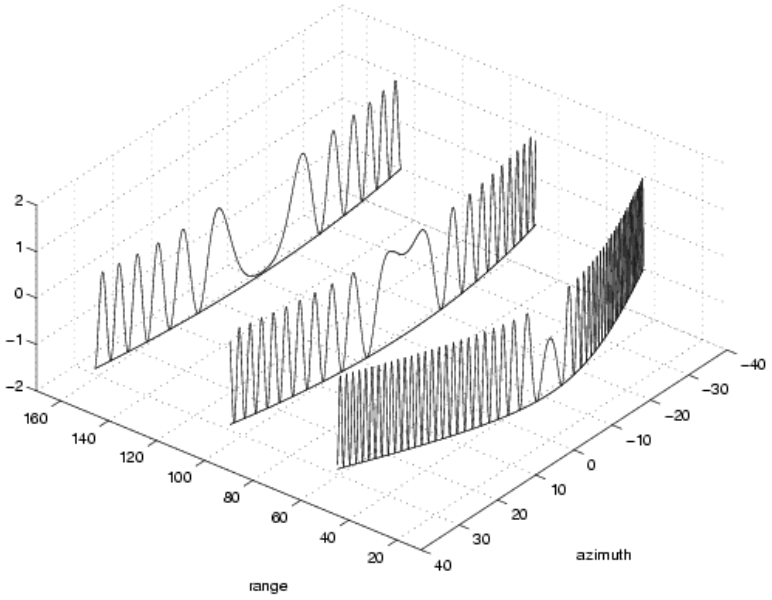

Figure 2.4: A visualization of the SAR signal model. The range dependent azimuth chirps are bent along the range dependent azimuth "smiles".

phase histories is what make exact SAR inversion a difficult problem. Often, the PSR function is normalized by substituting $\Delta R(r',x',x) = R(r',x',x) - r'$, the normalized range to target function, in for $R(\cdot)$.

Using the signal history of a single target in range compressed data, a data collection of many targets, $d(x,t)$, can be written then as a sum of the of scene

reflectivities, $\sigma(x', r')$ correlated with the PSR of Eq. (2.18),

$$d(x,t) = \int\int \sigma(x', r')\delta(t - \frac{2}{c}R(\cdot)) \exp\left[-j\omega_0 \frac{2}{c}R(\cdot)\right] dr'\, dx'. \tag{2.19}$$

To examine the model in a Hilbert space framework we take the Fourier transform of $d(x,t)$ in the time domain to obtain

$$d(x,\omega) = \int\int \sigma(x', r') \exp\left[-j(\omega + \omega_0)\frac{2}{c}R(r', x', x)\right] dr'\, dx'. \tag{2.20}$$

Equation (2.20) is an inner product of the target scene reflectivity function with the two-dimensional, non-orthogonal Green's function given by the $\exp(\cdot)$. Both types of functions exist in a L_2 space with the Green's function representing a basis onto which scene reflectivities are projected. The goal of a SAR processing algorithm is to invert this data model quickly and accurately to return the scene reflectivity.

2.5.2 Range-Doppler Algorithm

The first and most common SAR processing scheme is the Range-Doppler algorithm. In the SAR community, a common convention is to call the azimuth Fourier domain the "Doppler" domain. Hence, this processing method derives it's name from the fact that azimuth matched filtering is upon data that is Fourier transformed in the azimuth direction. The algorithm is often preferred because it makes approximations which simplify the azimuth matched filtering to multiple one-dimensional correlations. This effectively decouples range and azimuth dependences and creates a simplified processing problem. The algorithm can be summarized into three principle steps: range compression, a range-dependent RM correction and a quadratic approximation to the range-to-target function, $R(r', x', x)$, found in the $\exp(\cdot)$ of Eq. (2.19).

1. The first step is to perform range matched filtering. This operation is often done in the frequency domain to decrease processing time. This step yields data in the form found in Eq. (2.19).

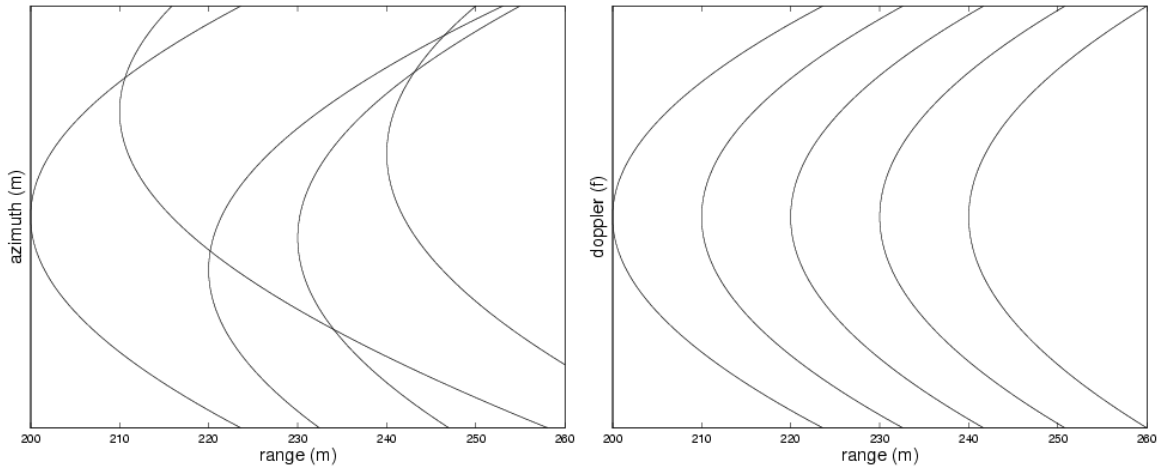

(a) (b)

Figure 2.5: Five target signal histories in the (a) range/azimuth and (b) range/Doppler domains

2. As illustrated in Fig. 2.5, each target in an imaged scene has a signal which is traced out along a range-dependent hyperbolic curve. To successfully decouple the range and azimuth dimensions, a correction is required that effectively straightens the "smiled" signal histories. This straightening of the curved signal histories cannot be done in the range-azimuth spatial domain due to the varying azimuth location of the loci of the target signal histories (see Fig. 2.5(a)). But when taken to the range-Doppler domain, $d(k_x, t)$, the transformed azimuth spectra loci become aligned as shown in Fig. 2.5(b), yet still retain their hyperbolic nature. Since the azimuth domain is a spatial domain, the Doppler wavenumber spacing Δk_x, is defined as

$$\Delta k_x = \frac{2\pi PRF}{v} \tag{2.21}$$

where PRF is the radar PRF, and v is the platform velocity.

3. Next, the curved histories in the range-Doppler domain are straightened by applying a k_x-dependent correction given by [8]

$$\Delta t(k_x, r) = \frac{2}{c} r\left(1 - \frac{1}{\sqrt{1 - (k_x c/(2\omega_0))^2}}\right), \tag{2.22}$$

which implies a range resampling or interpolation. It is noted that a high precision kernel must be used when performing this interpolation or undesired image artifacts may result. If the hyperbolic curvature is relatively constant with changes in range (i.e. $r \approx r_0$ a constant) then Eq. (2.22) can be evaluated with a single range for the entire image, and the interpolation simplifies to a phase multiplication applied in the two-dimensional Fourier domain [8]

$$\exp\left(-j\Delta t(k_x, r_0)\omega\right). \tag{2.23}$$

4. The final step in this algorithm is to apply an appropriate azimuth matched filter to the straightened signal histories. The newly straightened time domain data model is expressed as

$$d(x,t) = \int\int \sigma(x', r') \exp\left[-j\omega_0 \frac{2}{c} R(\cdot)\right] dr'\, dx'. \tag{2.24}$$

A common approach is to create a set of azimuth matched filters with each filter corresponding to a specific range in the image. This technique effectively sets the range variable in the data model, r', to a constant and simplifies the model down to multiple one-dimensional azimuth correlations. One of the matched filters with $r' = r_0$ can be written

$$d(x,t) = \int \sigma(x', r_0) \exp\left[-j\omega_0 \frac{2}{c} R(\cdot)\right] dx'. \tag{2.25}$$

This equation is easily solved using an azimuth matched filter for each range in the image. The exact matched filter, which accounts for the hyperbolic term in the azimuth chirp, is given by

$$\exp(j\omega_0 \frac{2R(r_0, x', x)}{c}) = \exp(j\omega_0 \frac{2}{c}\sqrt{r_0^2 + (x - x')^2}). \tag{2.26}$$

If the azimuth beamwidth is sufficiently narrow enough, a binomial expansion of the hyperbolic range-to-target function can be used:

$$R(r_0, x', x) \approx r_0 + \frac{(x - x')^2}{2r_0} + \cdots. \tag{2.27}$$

Employing only the first two terms of the expansion to form a quadratic approximation, the time-domain azimuth matched filter found in Eq. (2.26) simplifies to:

$$\exp(j\omega_0 \frac{2}{c}\sqrt{r_0^2 + (x - x')^2}) \approx \exp(j\omega_0 \frac{2}{c}(r_0 + \frac{(x - x')^2}{2r_0})). \tag{2.28}$$

Matched filtering is often done in the frequency domain for its computational ease and efficiency, and because the data is still in the range-Doppler domain.

This algorithm has been employed for many years; however, the approximations of Eq. (2.23) and Eq. (2.28) may create phase errors, which if neglected can cause unwanted image artifacts. These phase errors can be approximated and corrected for, but more processing and higher-order interpolators are required [6], [8]. Another drawback to the Range-Doppler algorithm is its inability to handle linear drift of target phase induced from squint or from the Earth's rotation. This linear drift, or range walk, of the signal history spreads the azimuth time bandwidth product (TBP) across multiple range bins. The effect of this spreading is lowered azimuth TBP in any specific range bin, which results in smearing the target in range. To correct for this drift, the data requires another range matched filter with an adjusted chirp rate. This second filter, known as secondary range compression, is often represented as being cascaded with the ideal range filter. Further information about this process and its effectiveness can be found in [6], [11], [12], and [13].

2.5.3 Wavenumber Domain Processing

The Wavenumber Domain algorithm, also known as the ω-k or spatial frequency interpolation algorithm, emerged in the early 1990's as a product of seismic migration techniques. The algorithm operates as if the radar has a stop-and-go motion. That is, the radar can be viewed as stationary during the time it transmits a pulse and receives the echo. The targets in the scene are modeled as sources which emit pulses sampled by the radar as it moves along the track. Since the SAR signal is a sampled version of the wavefront propagating from many sources, the image is formed when the data is "backpropagated" to each source [14].

It is noted [8] that the algorithm assumes that the image data is centered around a reference range (r_0) and a corresponding reference time (t_0). Any value can be chosen for the offsets, but the most commonly chosen reference range corresponding to the center of the target area. The new range with offset is given by $r' + r_0$.

Various derivations of this algorithm using the wave equation and Fourier analysis exist [14], [15]. The final result is the algorithm reduces the SAR inversion problem into two, two-dimensional FFTs, a phase multiply, and a non-linear interpolation. The computational cost derived from the precision of the frequency domain interpolation determines the speed of the algorithm. The SAR data model rewritten using the reference range is given by

$$d(x,t) = \int\int \sigma(x',r')\delta(t - \frac{2}{c}R(\cdot)) \exp\left[-j\omega_0 \frac{2}{c}R(\cdot)\right] dr'\, dx' \tag{2.29}$$

where $R(\cdot) = \sqrt{(r'+r_0)^2 + (x-x')^2}$. The range compressed SAR data in the frequency domain is

$$d(x,\omega) = \int\int \sigma(x',r') \exp\left[-j(\omega+\omega_0)\frac{2}{c}\sqrt{(r'+r_0)^2 + (x-x')^2}\right] dr'\, dx'. \tag{2.30}$$

As previously noted, the difficulty in inverting this equation is the coupling between the range and the azimuth dimensions. The idea behind the Wavenumber Domain algorithm is to change the non-orthogonal basis Green's function to an orthonormal basis to make the model easily invertible. Changing of basis function is done by interpolation in the two-dimensional frequency domain. The steps of the Wavenumber Domain algorithm are

1. As in the Range-Doppler algorithm, the raw SAR data is range matched filtered. The range compressed data then has the form of Eq. (2.29).

2. Next, the range compressed SAR data is converted to the two-dimensional frequency domain. This involves taking the azimuth Fourier transform of the data model in Eq. (2.30). Since this cannot be done analytically, the method of stationary phase is applied. The method is based on the fact that integrals with highly oscillating integrands do not add a significant contribution to the integral's result, allowing for approximations of the integrand to make the integral

solvable. From [16], the azimuth Fourier transform of the Green's function in Eq. (2.30) using stationary phase is given as

$$F_x[\exp[-j(\omega+\omega_0)\frac{2}{c}R(r'+r_0,x',x)]] \approx$$
$$A\exp\left[-j(r'+r_0)\sqrt{\left(\frac{2(\omega+\omega_0)}{c}\right)^2-k_x^2}\right]\exp[-jk_x x'] \tag{2.31}$$

where A is a scaling factor ignored. Using this approximation, the two-dimensional Fourier transform of the SAR data model of Eq. (2.30) is

$$D(k_x,\omega)=\int\int\sigma(x',r')\exp\left[-j(r'+r_0)\sqrt{\left(\frac{2(\omega+\omega_0)}{c}\right)^2-k_x^2}\right] \times\exp[-jk_x x']\,dr'\,dx'. \tag{2.32}$$

Next, the constants from Eq. (2.32) are factored from the integral and substitutions are made leaving

$$\begin{aligned} D(k_x,\omega) &= \exp[-jk_{r'}r_0]\int\int\sigma(x',r')\exp[-jk_{r'}r']\exp[-jk_{x'}x']\,dr'\,dx' \\ &= \exp[-jk_{r'}r_0]S(k_{x'},k_{r'}) \end{aligned} \tag{2.33}$$

where

$$k_{r'} = \sqrt{\left(\frac{2(\omega+\omega_0)}{c}\right)^2-k_x^2} \tag{2.34}$$
$$k_{x'} = k_x. \tag{2.35}$$

3. Next, Fourier transformed data is multiplied by the conjugate complex exponential in Eq. (2.33) which can be viewed as a spatial basebanding of the image frequency data [10]. This operation is viewed as

$$S(k_{x'},k_{r'})=\exp[jk_{r'}r_0]D(k_x,\omega). \tag{2.36}$$

4. The expressions in Eq. (2.34) and (2.35) are known as a Stolt mapping and suggest interpolation in the range frequency domain. The non-linearity of the mapping, however, requires unevenly spaced interpolation, with the accuracy

of the processor being dependent upon the interpolation kernel implemented. An approximation for unevenly spaced interpolation can be found in [10]. It is noted that some algorithms perform the phase multiplication step before the interpolation ([9], [10]), while others perform the multiplication step after interpolation ([14]). Yet, as was shown in [8], the two approaches are mathematically equivalent. Once the interpolation step is complete, azimuth bandpass filtering is applied to make adjustments for antenna pattern and for processing different image looks.

5. After this step the final image is obtained by taking a two-dimensional inverse Fourier transform of the data. The data is now azimuth compressed but lacks a scaling factor correction, which is described in [9].

While this algorithm produces little or no phase errors in final images, the required precision in interpolation makes this algorithm computationally expensive.

2.5.4 Chirp Scaling

The Range-Doppler and Wavenumber Domain algorithms have a tradeoff between the amount of required computation and the achievable phase accuracy. Both algorithms can be extremely accurate if no approximations of the azimuth chirp are used and if the interpolator used in both cases is of high enough order. In 1992 a new algorithm known as Chirp Scaling was developed to try to lessen the impact of this tradeoff [17].

The algorithm description provided here utilizes the time scaling principle as found in [18]. This principle states that large time-bandwidth LFM signals can have their phase centers slightly altered by modulating them with another LFM chirp with a slightly offset chirp rate. This scaling property is used to equalize the range-variant signal phase histories in SAR signals.

The algorithm differs slightly from the Range-Doppler and Wavenumber Domain algorithms in that it performs some of its operations on the data before it has been ranged compressed. As described in [17], if an LFM chirp is transmitted, the

received, raw signal history of a single point target at (r_0, x_0) is

$$d(x,t) = a(t - 2R/c)\exp\left[-j\pi\beta(t-2R/c)^2\right]\exp\left[-j\omega_0 2R/c\right] \tag{2.37}$$

where a is the signal envelope, β is the chirp rate, and $R(\cdot)$ is the range-to-target function.

1. The first step in the chirp scaling algorithm involves converting the raw data to the range-Doppler domain. This is done applying the principle of stationary phase [16] and yields

$$\begin{aligned} d(k_x,t) \approx a(t - 2R_f/c)\exp\left[-j\pi\beta_f(t-2R_f/c)^2\right] \\ \cdot\exp\left[-j2\omega_0/c\sqrt{1-(k_x/(2\omega_0 c))^2}\right]. \end{aligned} \tag{2.38}$$

   The first exponential in the expression represents the received range chirp while the second exponential represents the azimuth modulation (chirp). The chirp scaling algorithm moves around the need for interpolation by operating on the range chirp expression. The $R_f(\cdot)$ function describes the range migration of the data through the range Doppler domain and is given by

$$R_f(k_x, r_0) = r_0[1 + C_s(k_x)] \tag{2.39}$$

   where $C_s(k_x)$ is known as the curvature factor [17] given by

$$C_s(k_x) = \frac{1}{\sqrt{1-(k_x/(2\omega_0 c))^2}} - 1. \tag{2.40}$$

2. The next step removes the range dependence from the range curvatures by multiplying the range Doppler data by the chirp scaling multiplier

$$\Phi_1(r_0, k_x) = \exp\left(-j\pi K_s(k_x, r_0)C_s(k_x)[\frac{2}{c}(r - r_{ref})]^2\right). \tag{2.41}$$

   This expression ensures that all target phase histories effectively follow the curved trajectory given by the phase history at range, r_{ref}, thus removing the need for interpolation as needed in the range-Doppler and Wavenumber Domain algorithms. As mentioned in [17], it is important to note that while this multiplier adjusts the phase centers of all the target chirps, it does not change the location of the signal envelopes, $a(\cdot)$.

3. The next step is to convert the data to the two-dimensional Fourier domain by taking a range FFT. The expression then becomes

$$\begin{aligned} S(k_x,\omega) = a\left(\frac{\omega}{2\pi K_s(1+C_s(k_u))}\right) \\ \cdot \exp\left(-j2\omega_0/c\sqrt{1-(k_x/(2\omega_0 c))^2} - j\Theta(k_x,r)\right) \\ \cdot \exp\left(-j\frac{\omega^2}{4\pi^2 K_s(1+C_s(k_x))}\right) \\ \cdot \exp\left(-j\omega\frac{2}{c}(r+r_{ref}C_s(k_u))\right) \end{aligned} \tag{2.42}$$

where $\Theta(\cdot)$ is

$$\Theta(k_x,r) = \frac{4\pi}{c^2}K_s[1+C_s(k_u)]C_s(k_u)(r-r_{ref})^2. \tag{2.43}$$

The phase terms in Eq. (2.42) are the azimuth chirp, range chirp, and a linear phase term, respectively. The interpretation of each term is better described in [17] but the important change to note is the removal of the range dependence from the range chirp term.

4. The next step is to implement a bulk RM correction and range compression (including any secondary range compression). This is done now using the a single phase function that corrects the curvature for the reference range. The expression is given by

$$\Phi_2(k_x,\omega) = \exp\left(-j\pi\frac{\omega^2}{4\pi^2 K_s(k_u,r_{ref})[1+C_s(k_x)]}\right)\exp\left(j\omega\frac{2}{c}r_{ref}C_s(k_x)\right). \tag{2.44}$$

5. The next step is an inverse Fourier transform in the range direction. Once this is performed, the expression reduces to

$$d(k_x,t) = a(t-2r/c)\exp\left(-j2\omega_0/c\sqrt{1-(k_x/(2\omega_0 c))^2} - j\Theta(k_x,r)\right). \tag{2.45}$$

6. The signal in Eq. (2.45) contains the final phase function that requires matched filtering. The needed filter, along with a phase residual correction (from the chirp scaling), is

$$\Phi_3(k_x,t) = \exp\left(j2\omega_0/c\sqrt{1-(k_x/(2\omega_0 c))^2} + j\Theta(k_x,r)\right). \tag{2.46}$$

7. The final step is an inverse Fourier transform in the azimuth direction.

This algorithm proves advantageous over both range-Doppler and Wavenumber Domain processors since it preserves the phase history of the targets, yet does not require computationally costly interpolation. The only disadvantage of this algorithm is the large amount of memory required to process the raw SAR data and the fact that the algorithm is limited to radar systems that use LFM chirps as their transmit modulation. A few years after the development of Chirp Scaling, an improved version of the algorithm, known as Accelerated Chirp Scaling [19], was developed. This newer version utilizes range-compressed data and performs the chirp scaling operation not on the transmitted chirp, but on a chirp either introduced into the signal or upon a chirp inherent in the data (the chirp requiring secondary range compression). With these improvements, the new algorithm requires less memory to focus an image and has no limitations upon the transmit modulation scheme.

While all SAR processing algorithms strive to return the image reflectivity, some provide better results but at high computational cost and memory requirement. We now turn to an application of SAR images. One such application is to calculate the height of a target area by using two images of the same scene using what is known as interferometry.

2.6 Interferometry

The idea of determining scene topography from two observations originated with the area of stereometry. As seen from Fig. 2.6, stereometry uses two range observations, r_b and r_a offset by some baseline b to infer information in three dimensions about a target. Both observations have slightly differing ranges to the target and using basic trigonometry the height of the target can be inferred.

The height of the target can be found using the law of cosines [20],

$$r_b^2 = r_a^2 + b^2 - 2br_a \sin(\theta - \alpha). \tag{2.47}$$

The target height, h, is then found by the equation

$$h = H - r_a \cos(\theta). \tag{2.48}$$

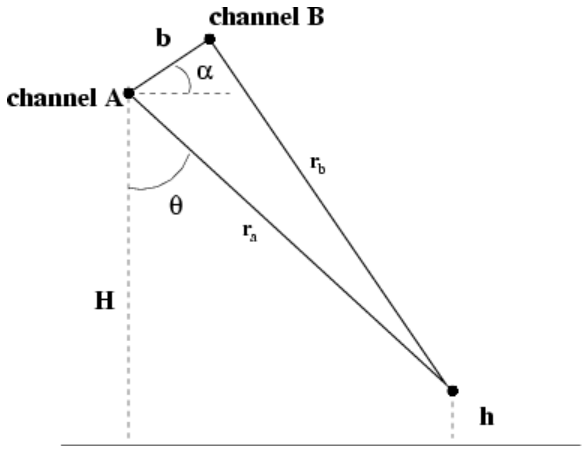

Figure 2.6: Stereometric geometry model

Typically, one of the ranges, the length of the baseline, and the height, H, are known exactly. This implies that the accuracy of the target height estimate, h is dependent upon the measurement of the second range, r_a, or upon the change in range Δr, which is defined as

$$\Delta r = r_b - r_a. \tag{2.49}$$

Graham [20] first proposed the idea of using the phase difference from two SAR images, slightly offset, to determine the value of Δr. The idea is that if one of the received SAR images has a signal given by

$$\gamma_1 = A_1 \exp\left(-j\frac{4\pi}{\lambda} r_a\right) \tag{2.50}$$

and a second SAR image, which is slightly offset from the first, has a signal of

$$\gamma_2 = A_2 \exp\left(-j\frac{4\pi}{\lambda} r_b\right), \tag{2.51}$$

then the phase difference

$$\Delta\phi = \arg\left[(\gamma_1)(\gamma_2)^*\right] = \frac{4\pi}{\lambda}\Delta r \tag{2.52}$$

enables estimation of the range difference, Δr. The accuracy of the estimate is related to the size of the wavelength and the size of the baseline, b. Two single-look complex

(SLC) SAR images, one from each channel, are used to make a phase difference image known as an interferogram. The phase differences contained in interferograms are initially wrapped between 0 and 2π and require two-dimensional phase unwrapping in order to find the Δr estimate.

The steps involved in performing interferometry to find a 3-dimensional height map of a target scene are:

1. First, a SAR image is created for each observation point. The two resulting images are slightly offset from each other. The image data is collected either by using a single-pass system with two receive antennas or by using a dual-pass system with one receive antenna. The important thing here is that the images are created with the highest possible phase accuracy (i.e., with the best SAR processing algorithm).

2. The next step is to assure that every complex data cell from one image corresponds to the same data cell in the other image. This process of image alignment of two SAR images is known as coregistration. This step is important because the less well coregistered the images are, the poorer the height estimates they produce. Often, the images must be reinterpolated to accurately coregister them. The quality of the interpolation determines the amount of phase error introduced in the interpolation [21].

3. An interferogram is created through the complex conjugate multiplication [Eq. (2.52)] of the two coregistered SLC images.

4. The phase differences obtained from the interferogram are wrapped from 0 to 2π. This next step is to unwrap the phase differences. Various two dimensional phase unwrapping techniques are found in [22]. Prior to phase unwrapping a variety of optional preprocessing steps can reduce phase noise. In [22], wrapped interferograms use coherent averaging or "multilooking" to remove noise. This lowers achievable resolution in the final interferogram, but reduces the multiplicative noise (or "speckle") inherent in SAR images. Another common filter

applied to interferograms is an averaging filter which smooths a data cell by averaging the pixels around it. This filter helps to remove Gaussian additive noise and is given by

$$\hat{\phi}_{mn} = \arctan\left(\sum \sin\phi_{ij}, \sum \cos\phi_{ij}\right) \tag{2.53}$$

where the data cell ϕ_{mn} is an average over a patch centered around (m, n).

The last common aid in phase unwrapping is the removal of a bulk "flat-earth" phase from the interferogram. The idea behind this preprocessing step is to remove the phase differential that corresponds to a flat earth scene. What remains after this flat-earth removal is a phase difference that corresponds to the topography of the ground with respect to the flat earth. Often, an estimate of the earth height is used to calculate a flat earth estimate. The final effect of flat earth removal is a reduction in the interferogram fringe rate which makes unwrapping significantly easier. However, once this topographical phase is unwrapped, the flat earth phase must be added back in to produce valid height estimates.

5. The last step is to geolocate the image targets using platform location data obtained during the flight (typically with GPS). Since the targets' slant ranges and heights above the reference flat earth are known, the position of the targets with reference to the platform can be known with some degree of accuracy. Further information on geolocation of targets can be found in [23].

Interferomtery has found many applications ranging from high-resolution digital elevation map (DEM) creation [23] to differential images using multiple interferograms [24].

2.7 YINSAR

Typically, interferometric SAR systems tend to be expensive and large. In 1995 Brigham Young University created a relatively small, low-cost interferometric synthetic aperture radar, YINSAR [25]. The X-band radar is a dual channel system,

Table 2.1: Common YINSAR parameters [1]

Parameter	Symbol	Value
Center Frequency	f_c	9.9 GHz
Time-Bandwidth Product	τB	300
Range Chirp Bandwidth	B	200 Mhz
Antenna Azimuth Beamwidth	θ_{az}	12°
Typical Platform velocity	v	60 m/s
Minimum PRF	PRF_{min}	629 Hz
Typical PRF	PRF_{min}	1000 Hz
Theoretical single look Range Resolution	δ_r	0.75 m
Theoretical single look Azimuth Resolution	δ_a	0.1 m

operating on two x86 processors. It's low-cost nature is achieved by using off-the-shelf A/D, D/A hardware and commercially built microwave circuits. It operates on board a Cessna Skymaster platform and has a peak transmit power of 10W, limiting the platform altitude. A table of key YINSAR parameters as from [1] are found in Tab. 2.1. While low transmit power and platform choice help to maintain a low overall cost, they both introduce large amounts of motion in the platform. Uncompensated motion in a SAR image induces image errors, and causes geometric inaccuracies.

The goal of YINSAR is two-fold: first, it is used create interferometric images. An area of particular interest is known as the Slumgullion slide, a landslide near Montrose, CO (Fig. 2.7). This natural landslide moves at a constant, predictable rate which has given it much attention by the U.S. Geological Survey (USGS). Until recently, surveys of the slide's movement have been a manual process using handheld GPS. The hope is that through YINSAR and differential interferometry, the slide's motion can be tracked with greater accuracy and improved resolution. The second goal of YINSAR is to aid archaeologists. With SAR, archaeologists can use radar imaging to aid in excavation and in the search for new sites. However, to attain the highest accuracy in these applications, motion compensation must be performed.

Figure 2.7: Slumgullion Slide near Montrose, CO [3].

Chapter 3

Motion Compensation

Since SAR processing algorithms assume a straight-line platform track and constant velocity, undesired platform motion can have adverse effects on images. To maintain geometrically accurate, focused, images the motion must be accounted for by either modifying the azimuth matched filters or by adjusting the data itself to make it optimal for conventional SAR imaging. Three main types of platform motion error degrade synthetic aperture radar images: translational motion errors, errors in platform attitude, and unequal PRF spacing due to a varying along-track velocity. This chapter is provided as a background to understand motion in SAR and is created from the compliation of various sources. Specifically, this chapter considers each of the three motion error sources, their effects on SAR, and some select methods of motion compensation (MOCO) used in literature.

3.1 Translational Errors

The first type of error, translational error, refers to platform position displacements from a straight-line track. The translational motion geometry of the platform at zero Doppler is seen in Fig. 3.1. These errors depend upon the range to each target and upon the reference height above the ground. Two primary results arise from these deviations. First, a phase error is introduced to all targets. This warps target phase histories and leads to image artifacts and geometric inaccuracies. Second, if the translational errors are large enough, they can cause target signatures to drift into neighboring range bins. The key to understanding these effects is to consider the effect of a displacement upon the range migration function.

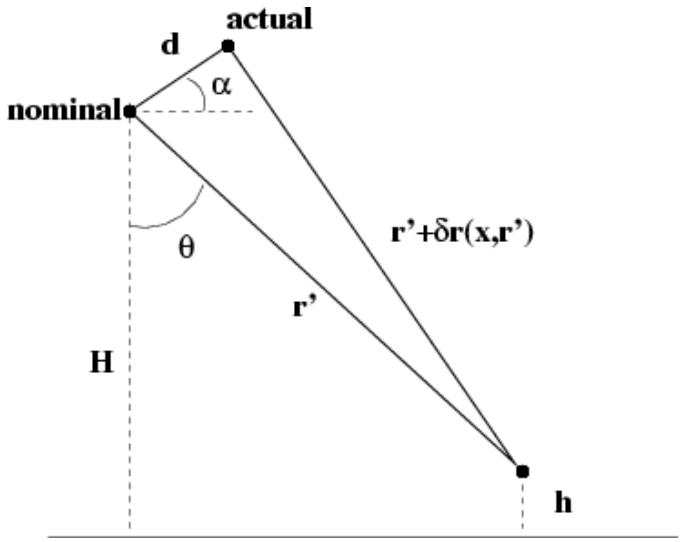

Figure 3.1: Displacement motion geometry at zero Doppler used to understand the effect of translational motion on SAR.

To modify the range migration function, R, to account for deviations, the near range displacement at zero Doppler, $\delta r(x, r')$, is needed. This is derived using the geometry in Fig. 3.1 and the Carnot Theorem [26] as

$$\delta r(x, r') = \sqrt{(r')^2 + d(x)^2 - 2d(x)r' \sin\left(\theta(x) - \alpha(x)\right)} \tag{3.1}$$

where x is the along-track position of the transmitting antenna, r' is the range to a target, and $d(x)$ is the cross-track antenna displacement. The angles θ and α are platform look and roll angles respectively. Applying the near range displacement to the range migration function results in the modified range migration function,

$$R_m(r', x', x) = \sqrt{(r' + \delta r(x, r'))^2 + (x - x')^2}, \tag{3.2}$$

which can be decomposed into two parts,

$$R_m(r', x', x) = R(r', x', x) + \delta R(r', x', x). \tag{3.3}$$

The $R(\cdot)$ function represents the nominal range migration function,

$$R(r', x', x) = \sqrt{r'^2 + (x - x')^2}, \tag{3.4}$$

and $\delta R(\cdot)$ represents the range migration displacement,

$$\delta R(r', x', x) = \sqrt{(r' + \delta r(x, r'))^2 + (x - x')^2} - \sqrt{r'^2 + (x - x')^2}. \tag{3.5}$$

The dependence of $\delta R(\cdot)$ on the azimuth target coordinate, x', determines the complexity of the motion compensation required.

Applying the modified range migration function of Eq. (3.3) to the SAR signal, yields

$$\begin{aligned} d(x,t) = \int\int \sigma(x', r') \delta(t - \frac{2}{c}[R(r', x', x) + \delta R(r', x', x)]) \\ \cdot \exp\left(-j\omega_0 \cdot \frac{2}{c}[R(r', x', x) + \delta R(r', x', x)]\right) dr'\, dx'. \end{aligned} \tag{3.6}$$

As seen in Eq. (3.6), range migration deviations have small effects on the range of the targets (the $\delta(\cdot)$ function), but can have greater effects upon the azimuth phase modulation function. Errors in range migration become significant when displacements are on an order of the range resolution, while any changes on the order of the transmit wavelength are significant in the phase modulation function.

In the frequency domain, Eq. (3.6) becomes

$$\begin{aligned} d(x,\omega) &= \int\int \sigma(x', r') \overbrace{\exp\left[-j(\omega + \omega_0)\frac{2}{c} R(r', x', x)\right]}^{g(r', x', x, \omega)} \\ &\qquad \times \underbrace{\exp\left[-j(\omega + \omega_0)\frac{2}{c}\delta R(r', x', x)\right]}_{m(r', x', x, \omega)} dr'\, dx' \\ &= \int\int \sigma(x', r') g(r', x', x, \omega) m(r', x', x, \omega)\, dr'\, dx'. \end{aligned} \tag{3.7}$$

This expression is a projection of the scene reflectivities onto a space spanned not only by the nominal Green's functions, $g(\cdot)$, but also onto a set of motion Green's functions, $m(\cdot)$. Any effects caused by $m(\cdot)$ depend upon the azimuth target coordinate, x'. This dependence can be seen through a binomial expansion of the range migration deviation

$$\begin{aligned} \delta R(r', x', x) &= \sqrt{(r' + \delta r(x, r'))^2 + (x - x')^2} - \sqrt{r'^2 + (x - x')^2} \\ &\approx (r' + \delta r(x, r')) \left(1 + \frac{(x - x')^2}{2(r' + \delta r(x, r'))^2}\right) - r' \left(1 + \frac{(x - x')^2}{2r'^2}\right) \\ &= \delta r(\cdot) - \frac{\delta r(\cdot)(x - x')^2}{2r'(r' + \delta r(\cdot))}. \end{aligned} \tag{3.8}$$

Thus, any dependence on x' is primarily due to the magnitude of the zero Doppler deviation, $\delta r(x, r')$.

When deviations are large enough, the higher-order terms introduce into the model what is known as range migrating phase error. This error, if uncompensated, can cause inaccuracies in the final image.

From an alternative perspective, the x' dependence of $\delta R(\cdot)$ can be viewed as a dependence upon the azimuth beamwidth. Often motion compensation is approached with vector analysis, with platform displacements represented as the magnitude of the difference between nominal and actual range-to-target vectors [1],[27]. Using the notation from the imaging situation in Fig. 3.2, the correction for a target at zero Doppler is given by

$$\mathbf{r}_{actual} - \mathbf{r}_{nominal} = \delta r(x, r'), \tag{3.9}$$

where $\mathbf{r}_{actual}$ and $\mathbf{r}_{nominal}$ are the nominal and actual range-to-target vectors. However, when considering the target at the edge of the azimuth swath (see Fig. 3.2), the deviation is given by

$$\mathbf{r}_{actual} - \mathbf{r}_{nominal} = \delta r(x, r') \cos(\theta_{az}/2), \tag{3.10}$$

where θ_{az} is the azimuth beamwidth. So while range migrating phase error is caused by large zero Doppler deviations, $\delta r(x, r')$, it can also be caused by a wide azimuth beamwidth, θ_{az}, even when platform deviations are small. For small deviations and a small azimuth beamwidth, the approximation $\delta R(r', x', x) \approx \delta r(x, r')$ (which assumes that all targets within the beam of the antenna have a zero Doppler deviation) is valid. This is known as the narrow azimuth beamwidth, or narrowbeam, approximation and is useful for understanding the effects of translational motion on SAR images.

3.1.1 Narrowbeam Approximation

The narrowbeam approximation is important for it makes the SAR signal model linear shift-invariant in azimuth and allows for insightful analysis of motion. With the narrowbeam assumption applied in the SAR motion model of Eq. 3.7, any

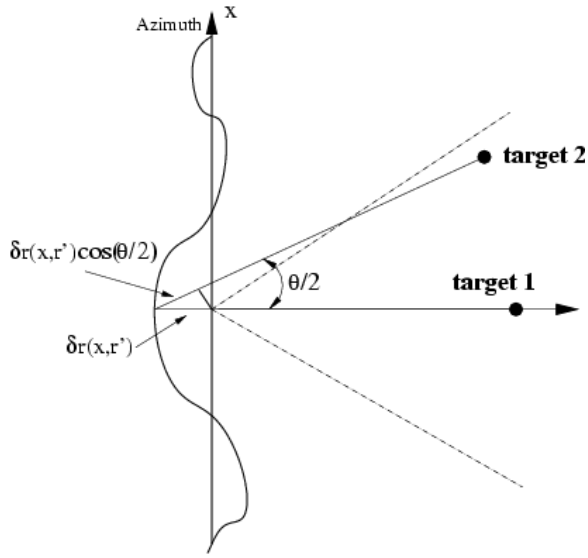

Figure 3.2: Two targets at the same range may require different motion corrections due to their azimuth location in the swath.

x' dependence is removed from the motion Green's function, $m(\cdot)$. The SAR model is then given as

$$d(x,\omega) = \int\int \sigma(x',r') g(r',x',x,\omega) m(x,r',\omega)\, dr'\, dx'. \tag{3.11}$$

Taking the Fourier transform of Eq. (3.11) in the azimuth direction yields a convolution of the two Green's functions in the Doppler wavenumber domain, k_x,

$$D(k_x,\omega) = \int\int \sigma(x',r') \left[G(x',k_x,r',\omega) \otimes_{k_x} M(k_x,r',\omega)\right]\, dr'\, dx'. \tag{3.12}$$

Applying the stationary phase principle to provide the Fourier transform of $G(x',k_x,r',\omega)$ and writing out the k_x convolution yields

$$D(k_x,\omega) = \int\int\int \sigma(x',r') G(\gamma,r',\omega) \exp\left[-j\gamma x'\right] M(k_x-\gamma,r',\omega)\, d\gamma\, dr'\, dx'. \tag{3.13}$$

Further simplification of Eq. (3.13) results in

$$\begin{aligned} D(k_x,\omega) &= \int\int \sigma(\gamma,r') G(\gamma,r',\omega) M(k_x-\gamma,r',\omega)\, dr'\, d\gamma. \\ &= \int \left[S(k_x,r') G(k_x,r',\omega) *_{k_x} M(k_x,r',\omega)\right]\, dr', \end{aligned} \tag{3.14}$$

where $S(k_x, r')$ represent an azimuth Fourier transformed version of the reflectivity function, σ. This demonstrates that in the case of a narrow beamwidth approximation, the effects of the translational motion on an image is simply the azimuth convolution of the nominal image spectrum with the spectrum of the motion Green's function. The effects on the final image then, depend upon the type of platform deviations experienced. The cases of linear and sinusoidal motion are discussed below and are also treated in [26].

Linear motion assumes that the radar platform is slowly drifting away from the nominal track at a constant rate, $a(r')$, over the length of the synthetic aperture, with the displacement function

$$\delta r(x, r') = a(r')x. \tag{3.15}$$

Inserted into the motion Green's function this expression gives

$$m(x, r') = \exp(-j(\omega + \omega_0)\frac{2}{c}a(r')x) \tag{3.16}$$

which has an azimuth Fourier transform of

$$M(k_x, r') = \delta(k_x + 2ka(r')). \tag{3.17}$$

Reevaluating the SAR model Eq. (3.14) with this motion function yields

$$D(k_x, \omega) = \int S(k_x - 2ka(r'), r')G(k_x - 2ka(r'), r')\, dr', \tag{3.18}$$

which is a range dependent Doppler shift of target spectra with the shift dictated by the magnitude of $a(r')$. In the final SAR image, this translates into a shift of the targets in the azimuth direction. An example of the effects of this motion can be seen in Fig. 3.3. In the case of sinusoidal motion, it is assumed that the motion of the platform is at least one period over the length of the synthetic aperture. The displacement function is of the form

$$\delta r(x, r') = a(r')\cos(\zeta x) \tag{3.19}$$

where $a(r')$ is the range dependent amplitude and ζ is the spacial frequency of the motion. Following the same approach used with linear displacement, the motion

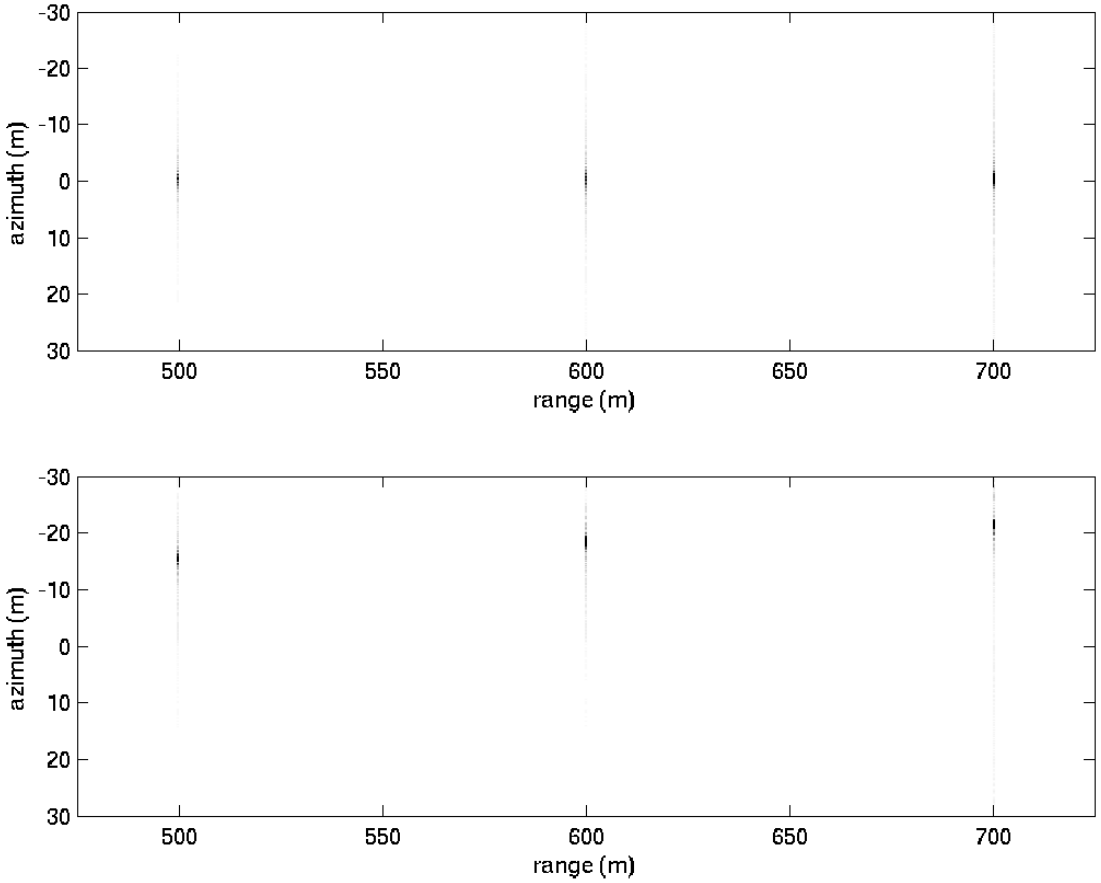

Figure 3.3: Three simulated targets in the presence of linear motion. Without motion(top). With motion(bottom). Note the range-dependent azimuth shift of the targets.

Green's function is

$$m(x, r') = \exp(-j(\omega + \omega_0)\frac{2}{c}a(r')\cos(\zeta x)). \tag{3.20}$$

Applying the Jacobi-Anger expansion [28],

$$\exp(iz\cos(\theta)) = \sum_n (i)^n J_n(z)\exp(in\theta), \tag{3.21}$$

the azimuth Fourier transform of the motion Green's function becomes

$$M(k_x, r') = \sum_n (-j)^n J_n((\omega + \omega_0)\frac{2}{c}a(r'))\delta(k_x - n\zeta), \tag{3.22}$$

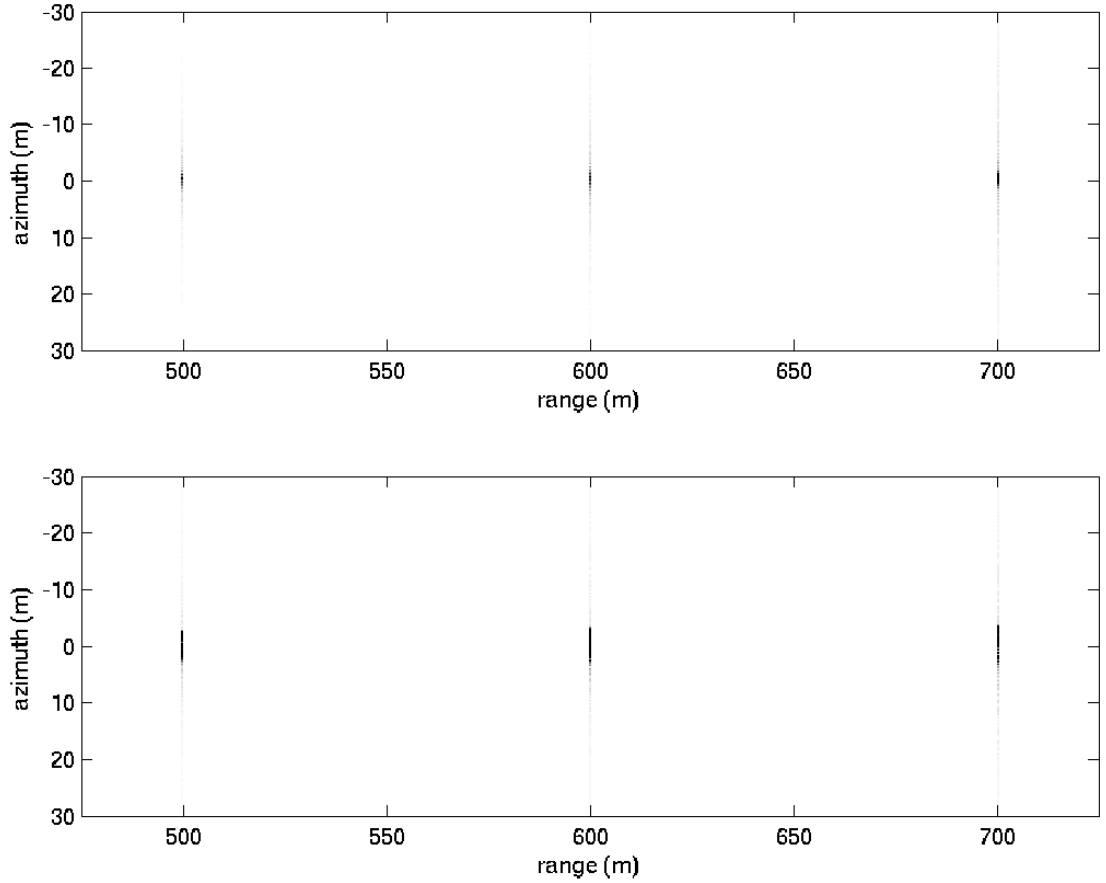

Figure 3.4: Three simulated targets in the presence of sinusoidal motion. Without motion (top). With motion (bottom). Note the range-variant azimuth smearing of the targets.

where J_n is an nth order Bessel function. Evaluating the SAR signal model with this expression results in

$$D(k_x, \omega) = \sum_n \int (-j)^n J_n((\omega + \omega_0)\frac{2}{c}a(r'))S(k_x - n\zeta), r')G(k_x - n\zeta, r')\, dr'. \quad (3.23)$$

Thus, in the case of sinusoidal motion, the azimuth frequency domain consists not only of the main target spectrum but also with shifted copies of itself that have been scaled by a Bessel function. The magnitude of the copies is dictated by the amplitude of the sinusoidal deviations. An example of the effects of this kind of motion can be seen in Fig. 3.4. Although a narrowbeam approximation gives useful insight into the effects of translational motion on a SAR image, the effects of large deviations or a

wide azimuth beamwidth cannot be analyzed in this fashion. Widebeam situations can be corrected; however, the motion compensation complexity increases.

3.2 PRF Spacing Errors

The second type of motion errors occur when the along-track velocity of the platform changes while the radar collects with a constant PRF. In terms of a phased array, this error represents an unequal spacing between phased array elements. This error lowers the focusing of the synthetic aperture and, if the spacing error is too large, can introduce image artifacts. The correction of these types of errors is generally straight-forward and requires interpolation of the complex image in the azimuth direction.

3.3 Attitude Errors

The last type of motion errors are those in platform attitude which are variations in yaw, pitch, and roll. These errors generally produce negligible amounts of range displacement and primarily effect the gain of the SAR image. If the attitude error is purely one of roll, as shown in Fig. 3.5(a), the principle effect is only a change in the gain of the image. Variations of either pitch or yaw of the platform, as seen in Figs. 3.5(b) and 3.5(c), steer the antenna beam ahead or behind the imaged area in the azimuth direction, with the yaw being range dependent. This squinting of the beam causes a frequency shift in the azimuth power spectrum of the received data that may or may not be range dependent. The magnitude of the frequency shift is a parameter known as the Doppler centroid. Once this value is known (usually through estimation), the center frequency of the azimuth matched filter is adjusted for the squint. Any gain problems introduced through variations in roll must be corrected through a rescaling of the complex SAR image.

3.3.1 Doppler Centroid

As was mentioned, the Doppler centroid is the frequency (or spatial wavenumber) corresponding to the center of the signal's energy centroid (power spectrum)

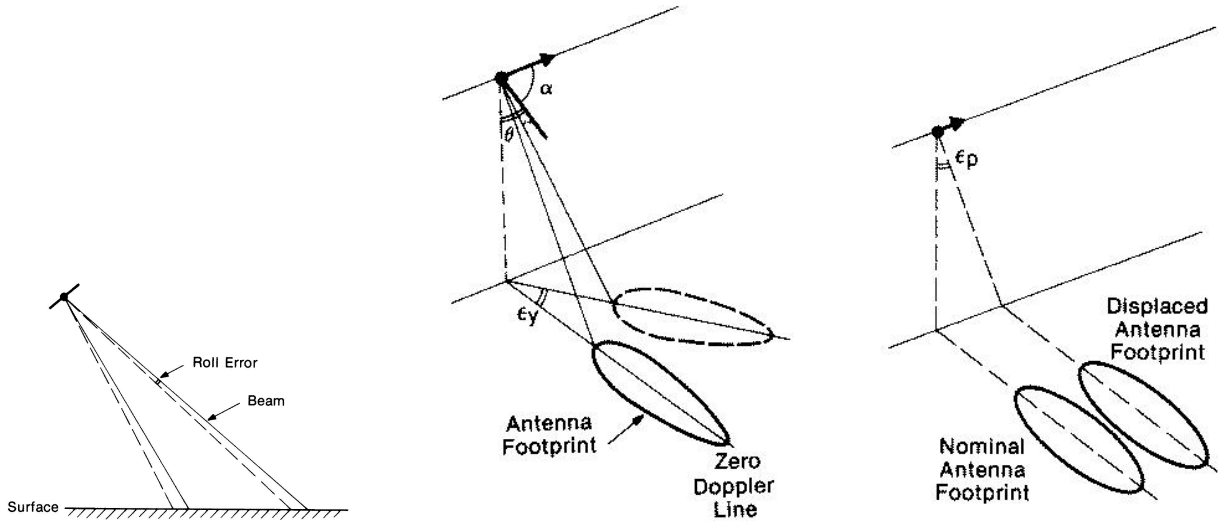

(a) (b) (c)

Figure 3.5: Attitude errors. (a) Roll error. (b) Yaw error. (c) Pitch error. (These figures were obtained from [4])

and is often range dependent. A shift in this spectrum results from a modulation caused either by a squint of the antenna away from zero Doppler or from a linear drift of the platform away from the nominal track in a narrowbeam SAR system. Aliasing of the azimuth spectrum occurs when the radar PRF is too low with respect to the platform velocity. This can be viewed as the azimuth power spectrum being undersampled by the PRF. Untreated aliasing in SAR images can cause artifacts and make estimation of the Doppler centroid difficult. Fortunately, it can be corrected by increasing the azimuth sample rate through the interleaving of zeros in the raw data [29]. If the data has an unaliased azimuth spectrum, the primary purpose of having a Doppler centroid estimate is to modify the size of the azimuth matched filter for computational efficiency. This parameter can be estimated from the motion data of the platform, but is limited by the accuracy of the attitude data. Most often it is estimated directly from the raw data. Various estimation schemes exist [30], yet the most common is frequency domain correlation.

3.3.2 Frequency Domain Correlation

Frequency domain correlation estimation uses the azimuth power spectrum of the complex data to estimate the Doppler centroid value. An azimuth spectrum estimate is obtained by creating a periodogram of the raw SAR data in the azimuth direction. Commonly, the variance of the azimuth periodogram estimate is lowered by averaging periodograms from multiple range bins. Next, it is correlated with a weighting function to determine the frequency shift. The Doppler centroid estimation with some centroid offset f_{DC}, is given as

$$C(f_{DC}) = \sum_{i=1}^{N} S(i) \cdot W(i\Delta f - f_{DC}) \tag{3.24}$$

where $S(i)$ is the SAR azimuth spectrum estimate and $W(\cdot)$ is the weighting function [31]. The Doppler centroid estimate is found where $C(f_{DC}) = 0$. In typical detection situations where a signal is buried in additive Gaussian white noise, the optimal value is found as the maximum from the correlation of the signal with the nominal signal function. However, in the case of multiplicative noise in SAR (due to speckle), finding the minimum with the appropriate weighting function is better for computational speed. The Doppler centroid estimator that achieves the Cramér Rao bound [31] uses the optimal weighting function,

$$W(f) = \frac{A'(f)}{A(f)^2}, \tag{3.25}$$

where $A(f)$ is the nominal azimuth spectrum. While this estimator produces optimal estimates, the SAR image contrast from large scatterers centered away from zero Doppler can cause errors. These errors arising from strong azimuth chirps located away from zero Doppler are avoided by an azimuth precompression of the data. Once Doppler centroid estimates are obtained for the entire image, they can be used later for increasing the average SNR for a SAR image by adjusting the center frequency of the azimuth matched filters.

3.4 Motion Compensation

While all motion errors have adverse effects upon SAR images, the primary source of error is due to undesired platform displacements. The choice of MOCO

algorithm depends upon the magnitude of these errors and the size of the azimuth beamwidth.

To perform any motion compensation, we need to know the position of the platform to calculate pertinent values such as $\delta r(\cdot)$, the Doppler centroid, etc. Most often the position is acquired using data from motion measurement devices such as GPS, accelerometers, and gyros. The displacement, $\delta r(\cdot)$, is typically estimated using a flat earth model or can also be estimated from the data itself with a technique known as the Reflectivity Displacement Method [32]. The Doppler centroid can also be estimated from the motion data [33], but is most often estimated directly from the raw data. In this section we assume these values are known or have been previously computed.

3.4.1 Narrowbeam Motion Compensation

The simplest type of motion compensation is best-suited for narrowbeam systems and assumes all corrections are not dependent upon the target azimuth coordinate, x'. The narrowbeam algorithm, which operates on range-compressed data, has four steps.

1. The direct motion compensation begins with a slant range dependent phase correction

$$\exp\left(j\omega_0 \frac{2}{c}\delta r(x, r')\right). \tag{3.26}$$

2. Next, the drifting of targets into other range bins must be corrected. If there is a negligible amount of slant range dependence on the deviations, such as in a satellite platform, then the approximation $\delta r(x, r') \approx \delta r(x)$ holds and a simple range bin shift can be applied. This range shift is often coupled with the phase correction and applied as a single multiplication step in the range-Doppler domain by

$$\exp\left(j(\omega_0 + \omega)\frac{2}{c}\delta r(x)\right). \tag{3.27}$$

However, in cases where there is a significant amount of slant range dependence, such as in a SAR with a wide range swath, range bins cannot be shifted. They require a resampling which must be done with enough precision to preserve phase information [1]. A good interpolation scheme is a multiple point sinc interpolator [2].

3. Next, any variations of Doppler centroid are accounted for by adjusting the center frequency of the azimuth matched filters in the range-Doppler domain to increase the average SNR of the final image.

4. Finally, any unequal spacing due to variations in the along track velocity coupled with a constant PRF are corrected by interpolation in the azimuth direction. Similarly, to maintain high phase accuracy, the interpolation must be a higher-order interpolator. This step could also be performed at the beginning of the motion compensation process with minimal error in the results [26].

This process motion compensates narrow beamwidth SAR data, including data with a slant range dependence. This approach makes the assumption that platform deviations from the nominal track are small enough that any x' dependence can be removed. Unfortunately, in many situations deviations from a nominal track are large and the motion compensation algorithm must include higher-order corrections.

3.4.2 Second-Order Narrowbeam Motion Compensation

In many SAR situations the narrowbeam approximation does not hold due to the large magnitude of platform deviations. As discussed in the previous section, large deviations introduce a dependence upon x', which causes range migrating phase errors. A common approach to deal with these situations is to decompose the platform deviations into range-dependent ($\delta_v r(x, r')$) and range-independent ($\delta_{r_0}(x)$) components [26], [33]

$$\delta r(x, r') = \delta_{r_0}(x) + \delta_v r(x, r'), \tag{3.28}$$

resulting in what is known as a first- and second-order motion corrections. The following algorithm operates upon range compressed data and attempts to make the system appear narrowbeam.

1. The first step in higher-order motion compensation is to apply what is known as first-order or bulk motion compensation. This correction, called a narrowbeam correction [9], is a bulk phase and range bin shift with respect to a specific reference range, r_0. A commonly chosen reference range is the center of the image. The correction is reduced down to a phase multiplication

$$\exp\left(j\omega_0\frac{2}{c}\delta_{r_0}r(x)\right) \tag{3.29}$$

   and a range bin shift

$$\exp\left(j\omega\frac{2}{c}\delta_{r_0}r(x)\right). \tag{3.30}$$

   Both operations are typically applied as a single multiply on the range Fourier transformed data. This correction, while not completely correct, puts the data in approximately the correct location [34]. The idea is that when bulk deviations are compensated, the system is reduced to a narrowbeam equivalent and that any range migrating phase errors are considered negligible.

2. Next, after applying a range migration correction from one of the azimuth processing algorithms, the residual motion deviations, $\delta_v r(x, r')$, are applied. The correction here is simply a multiplication of the data by the phase correction

$$\exp\left(j(\omega_0+\omega)\frac{2}{c}\delta_v r(x,r')\right). \tag{3.31}$$

   If the data is slant-range dependent, the bins may also need to be resampled to account for any range dependence.

3. Next, variations of Doppler centroid are accounted for by adjusting the center frequency of the azimuth matched filters in the range-Doppler domain to increase the average SNR of the final image.

4. The final step in this algorithm is to correct any faulty PRF spacing by resampling the motion compensated data in the azimuth direction. As was mentioned in the previous algorithm, this step could have been performed at the beginning of this algorithm.

This algorithm functions fairly well in reducing any range migrating errors that may be introduced into a narrow azimuth beamwidth SAR system by large deviations from a nominal track. However, in some instances the assumption that a SAR model can be reduced to narrowbeam is not valid. It is in these cases that motion compensation needs to be done pixel-by-pixel.

3.4.3 Widebeam MOCO

The assumption of a narrow azimuth beamwidth supports the idea that the deviations in the broadside direction are the same for all targets in the beam. This allows the removal of the target azimuth coordinate dependence from the deviation function and enables easier motion compensation. Unfortunately, in cases where a SAR has a wide azimuth beamwidth, the motion deviation may have a target azimuth position dependence, even when platform deviations are small. This effect is visualized in Fig. 3.2 where the target at the leading edge of the azimuth beam requires a smaller correction than the target located at zero Doppler. In considering a narrow beam SAR system the motion compensation procedure outlined in the previous section above works acceptably, however in the case of a system with a wide azimuth beamwidth the method must be modified. The following approach is used for widebeam motion compensation.

1. In [10] the problem is approached by applying the same first-order motion compensation as shown in Eq. (3.29) and Eq. (3.30). This shifts the data to an approximately correct location, minimizing the effects of range-varying phase error.

2. The next step is to azimuth compress the image and apply a phase correction. Due to the spatially varying nature of the data this correction is a target dependent filter that is most efficiently applied in the two-dimensional Fourier domain. The filter for a target at (x', r') is given by

$$H(k_{x'}, k_{r'}) = \exp\left(j2k\delta r_v(x, r')\right) \tag{3.32}$$

where

$$\begin{aligned} 2k &= \sqrt{k_{r'}^2 + k_{x'}^2} \\ x &= x' - \frac{k_{x'}}{k_{r'}} r' \end{aligned} \tag{3.33}$$

and where $\delta r_v(x, r')$ is the residual motion error after the first-order motion correction. The primary difficulty behind this algorithm is the large amount of computation required when dealing with a new filter for every target.

In [34], the approach is slightly modified to help improve the overall computation time. In this modified approach, the same first-order correction is applied, but the target-dependent phase correction is done in patches or segments rather than for each target. The correction for an entire patch is chosen to be the correction for a target at the patch center. All other targets in the patch need a slight phase correction, but this can be done using an analytic expression.

3.5 YINSAR Motion Compensation

The motion compensation algorithm for BYU's interferometric synthetic aperture radar was initially developed by Richard Lundgreen in 2001. The motion of the radar platform is determined by using two differential GPS units that sample positions at 5 and 10 Hz respectively, an accelerometer and gyros that sample at 500 and 1000 Hz, and a kinematic GPS that samples attitudes at 5 Hz. The primary difficulties are the synchronization of the various motion data streams, the removal of accelerometer and gyro biases, and the conversion of all different data types to the same spatial frame. All these problems are discussed by Lundgreen [1]. Because

YINSAR operates on a low-altitude aircraft and with a large range swath, the translational displacements are highly range dependent. These displacements, $\delta r(x, r')$, are calculated using estimated range values from a flat earth estimate. A single nominal track is used for the entire duration of each flight and a narrowbeam motion compensation is applied to range-compressed YINSAR data. The algorithm consisted of the following steps [1]:

1. First, the range dependent phase correction

$$\exp\left(j\omega_0 \frac{2}{c} \delta r(x, r')\right) \tag{3.34}$$

   is applied to all targets.

2. Next, due to the range dependent nature of $\delta r(x, r')$ an unevenly spaced interpolation is performed in the range direction using a cubic spline interpolation scheme.

3. The final correction is an azimuth interpolation of the data to correct for unequal PRF spacing. Cubic spline interpolation is used here.

The algorithm was originally written in Matlab and later translated to C. The motion compensated images are generally improved compared to uncompensated data. As can be seen in the images in Fig. 3.6, details become more distinct and images are more geometrically correct. While the quality of the motion compensated images improve, the motion compensated interferograms are slightly degraded. Compensated interferograms tended to be slightly more decorrelated than the uncompensated interferograms. This suggests the need for improved motion compensation when dealing with an interferometric system like YINSAR.

3.6 Interferometric Motion Compensation

When applying motion compensation in interferometric SAR, an accurate phase correction is required as it has a direct effect on the height estimation. To obtain accurate phase corrections, the terrain height needs to be exactly known;

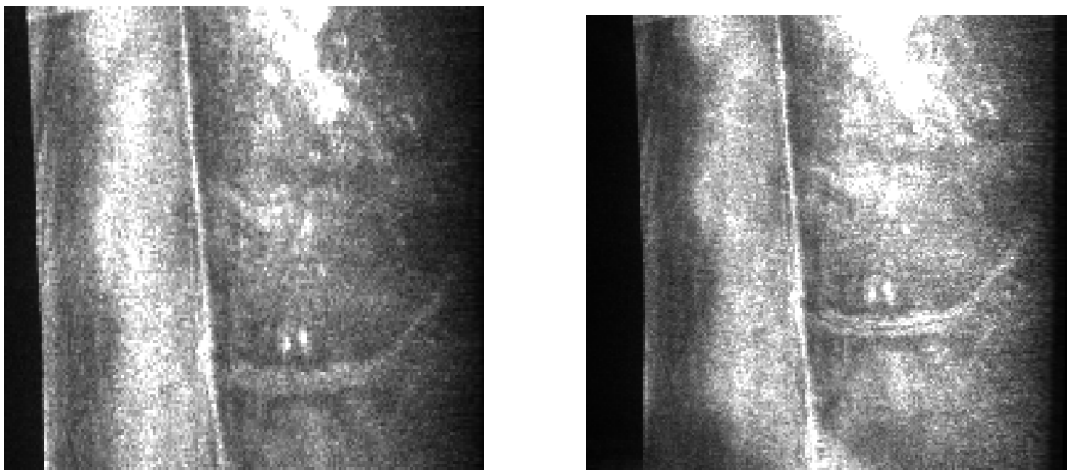

(a) (b)

Figure 3.6: YINSAR flight R, image 1300. (a) Before motion compensation and (b) after motion compensation.

however, this fact reveals a circular problem because the height is what is being estimated. This problem is typically approached with a flat earth estimate as in typical non-interferometric SAR. A commonly used geometric model is two-channel interferometric SAR with one monostatic channel (transmit and receive) and one bistatic channel (receive only). Two options are available for motion compensation for this interferometric SAR model. The first is to motion compensate each channel to a single reference track while the other is to motion compensate each channel to its own reference track. Both assume each channel has the same reference height, and both have distinct advantages and disadvantages [5] [35]. This geometric model is useful because it allows one of the channels to be independent of the look angle and results in an exact solution for the height estimate. The motion compensation assumed here is a narrowbeam compensation and that consists only of a phase correction. These assumptions make the analysis of the differential phase easy to perform and give insightful results.

3.6.1 Single Reference Track

With a single reference track, both channels are both compensated to the same nominal track with a single reference height. Due to a narrowbeam approximation,

the differential phase is zero whenever the range of the target at a certain height is equal to the flat earth range. The geometry of the single reference track is shown in Fig. 3.7(a). The applied and ideal motion compensated phase of the two images is

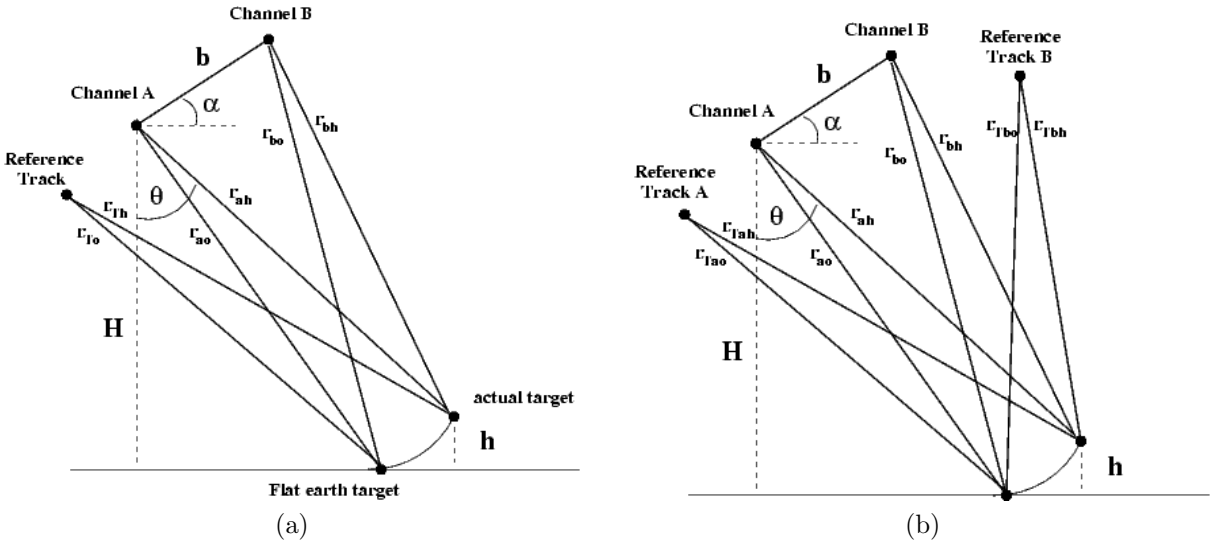

Figure 3.7: (a) Single and (b) double track geometry found in [5].

given as [35]

$$\phi_A(applied) = -\frac{2\pi}{\lambda}(2(r_{to} - r_{ao})) \tag{3.35}$$

$$\phi_B(applied) = -\frac{2\pi}{\lambda}((r_{to} - r_{ao}) + (r_{to} - r_{bo})) \tag{3.36}$$

$$\phi_A(ideal) = -\frac{2\pi}{\lambda}(2(r_{th} - r_{ao})) \tag{3.37}$$

$$\phi_B(ideal) = -\frac{2\pi}{\lambda}((r_{th} - r_{ao}) + (r_{th} - r_{bh})) \tag{3.38}$$

and the resulting differential phase is given by

$$\begin{aligned} \Phi_S &= \phi_A(applied) - \phi_A(ideal) - \phi_B(applied) + \phi_B(ideal) \\ &= -\frac{2\pi}{\lambda}(r_{bo} - r_{bh}). \end{aligned} \tag{3.39}$$

As is discussed in [5], this differential phase is used to find a height estimate of the target using known data. The height estimates found [5] by

$$h = H - r_{ao}\cos(\theta) \tag{3.40}$$

where

$$\theta = \sin^{-1}\left(\frac{\left(\frac{\lambda}{2\pi}\Phi_S + r_{bo}\right)^2 - b^2 + r_{ao}^2}{2br_{ao}}\right) - \alpha. \tag{3.41}$$

The main advantages to the single track approach are: first, flat earth fringes are automatically removed from the interferogram and, second, no discontinuities are present in the differential phase even if the nominal track is segmented over the entire flight. Unfortunately, a single reference track increases the chance of range migrating phase error (i.e., a dependence upon the azimuth position, x'). Any range migrating error in either of the two images introduces a bias in the final interferogram and causes a spectral shift in the data. An alternative to using a single track is to motion compensate each channel to its own ideal track.

3.6.2 Double Reference Track

With a double reference track, each channel is motion compensated to its own nominal track with both tracks having the same reference height. The same narrowbeam approximation is also assumed in the double reference track approach, with the differential phase being zero whenever the range of the target at some height is equal to the flat earth range. The geometry of the double reference track is shown in Fig. 3.7(b). As discussed in [5], the interpretation of the dual track differential phase is similar to that of dual pass imaging except for the phase difference

$$\Phi = -\frac{2\pi}{\lambda}(r_{ah} - r_{bh}). \tag{3.42}$$

Using a similar approach to that of Eqs. (3.35)-(3.38) the applied and ideal motion compensated phase of the two channels is given by

$$\phi_A(applied) = -\frac{2\pi}{\lambda}(2(r_{to} - r_{ao})) \tag{3.43}$$

$$\phi_B(applied) = -\frac{2\pi}{\lambda}((r_{tao} - r_{ao}) + (r_{tbo} - r_{bo})) \tag{3.44}$$

$$\phi_A(ideal) = -\frac{2\pi}{\lambda}(2(r_{tah} - r_{ao})) \tag{3.45}$$

$$\phi_B(ideal) = -\frac{2\pi}{\lambda}((r_{tah} - r_{ao}) + (r_{tbh} - r_{bh})). \tag{3.46}$$

Adding the phase difference between the ideal tracks (Eq. 3.42) to the resulting differential phase of the double track approach is given by

$$\Phi_S = -\frac{2\pi}{\lambda}(r_{tao} - r_{tbo} + r_{bo} - r_{bh}). \tag{3.47}$$

As mentioned in [5], when this differential phase is combined with known data an exact estimate of the target height above the reference flat earth can be created. The primary advantage to this method is its insensitivity to range migrating phase errors, as each channel has its own nominal track which minimizes translational deviations. Unfortunately, while reducing the amount of range-varying phase error, the dual track method does not share the advantages of removing the flat earth phase or the ability to handle track segmentation as does the single track approach. A combination of the two approaches is described in [5] and [35]. It first applies motion compensation using dual tracks to reduce range varying phase error, and after range migration correction and azimuth compression, converts the data to a single track form by the phase correction

$$\phi = -\frac{2\pi}{\lambda}(r_{tao} - r_{tbo}). \tag{3.48}$$

This correction effectively motion compensates one of the channels onto the other channel and makes the resulting differential phase similar to that of the single track. While both single and dual track methods function well for the suggested geometric model (with one channel bistatic, one channel monostatic), it must be modified in the case of BYU's interferometric synthetic aperture radar to account for both of its bistatic channels.

Chapter 4

YINSAR Motion Compensation

4.1 Overview

One of the primary goals of this thesis is to evaluate the effectiveness of the current YINSAR motion compensation algorithm and make improvements upon it. The narrowbeam MOCO algorithm prescribed by Lundgreen can be improved in its ability to deal with high Doppler centroid variations, through either a higher-order motion compensation algorithm or a segmented reference track, and by considering the effects of motion compensation on a bistatic interferometric system using the analysis of [5].

4.2 YINSAR Processing

Due to the narrow azimuth beamwidth of YINSAR and memory limitations, a data collection is commonly processed in subimages. The first processing step is range compression of the received radar data using a fast correlation method. Due to memory limitations, only a segment of range compressed lines are loaded into memory for azimuth compression, creating a smaller subimage. The final SAR image is created by connecting together multiple subimages. A byproduct of creating a large SAR image from many smaller images can be a light/dark periodic banding caused by gain variations due to platform roll and the antenna pattern. If the pattern and roll are known, a compensation can be applied [20]. Otherwise, the data is processed in an overlap/save overlap/add method. The amount of overlap is a tradeoff between the

amount of tolerable azimuth banding in the image and the amount of extra processing required.

Image segmentation also needs to be considered during motion compensation. When a single reference track is used for an entire flight, all motion corrections can be applied to the range compressed data prior to azimuth compression. This approach requires less computation and is typically less complicated to implement. On the other hand, when a segmented reference track is used, motion corrections for each range line can change with each new segment to be processed. The computation time increases with increasing overlap between image segments during azimuth compression.

4.3 Doppler Centroid

The first area of motion compensation improvement is to make adjustments for variations in Doppler centroid. The Doppler centroid can range from a fairly constant value to being highly variant due to platform instability. The primary concern in estimating the Doppler centroid is to know when azimuth spectrum aliasing occurs. When azimuth compressed, an aliased spectrum introduces undesired artifacts into the image. If the azimuth spectrum is unaliased, then the effects of a non-zero Doppler centroid can be compensated for.

For YINSAR, the Range Doppler azimuth compression algorithm prescribed by Thompson [25] limits the processed azimuth bandwidth to minimize the need for range migration correction. A consequence of the narrowed Doppler bandwidth is that any non-zero Doppler centroid reduces the SNR of the processed image. These changes in SNR create dark/bright azimuth bands or strips in the final image (e.g. Fig. 4.1). Yet, if the passband of the azimuth matched filters is increased to better handle more variation in the Doppler centroid, then a range migration correction is necessary.

Due to YINSAR's narrow beamwidth and low imaging altitude, its range migration through cells is limited, but not negligible. The range migration in the current YINSAR processing scheme is eliminated by zeroing out the higher portions of the

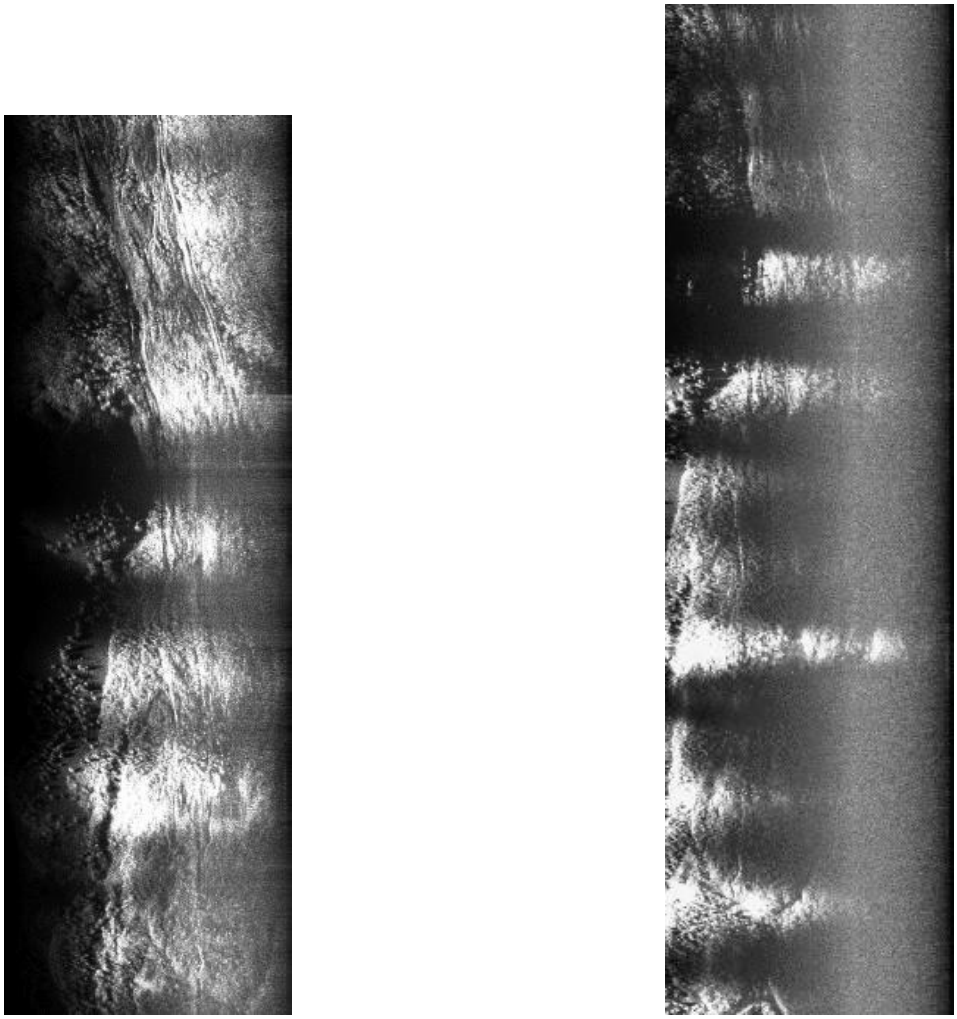

(a) (b)

Figure 4.1: Azimuth Banding seen in Flights (a) 2209 and (b) 0717 due to excessive Doppler centroid and a small azimuth passband.

Doppler bandwidth. This removes the need for a range migration correction, but leads to lower azimuth resolution and is problematic for variations in Doppler centroid.

The YINSAR range Doppler algorithm was modified to include a range migration correction as described in Section 2.5.2. Cubic spline interpolation is used in the resampling to help preserve phase. An example of the corrected range Doppler data is seen in Fig. 4.2.

After correcting for range migration, the azimuth processing bandwidth can be increased. These changes in processing produce two benefits: first, azimuth resolution

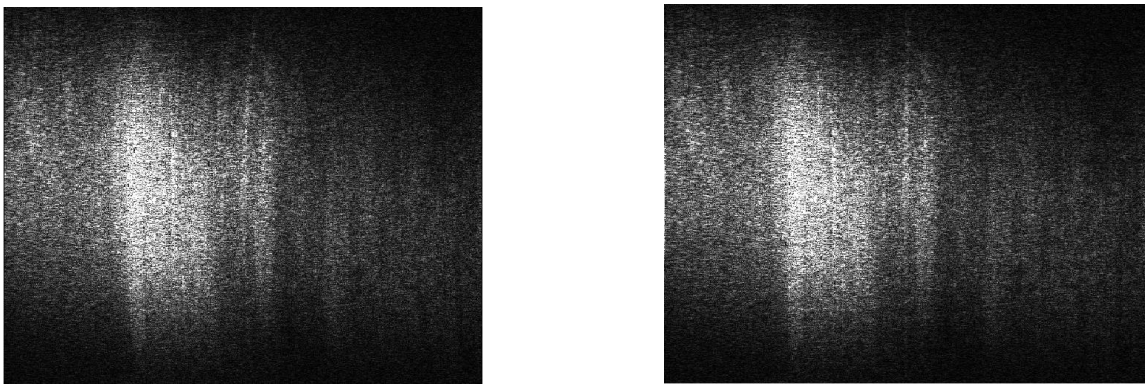

(a) (b)

Figure 4.2: (a) Range migrated Range Doppler SAR data from flight 2209 (Note the moon-like curvature along the vertical axis) and (b) the same data with the range migration corrected (note the corrected curvature).

improves (e.g. Fig. 4.3). Second, light/dark azimuth banding in the final image is reduced. However, a larger azimuth bandwidth can introduce undesired artifacts into an image if the Doppler spectrum is aliased.

When an aliased azimuth spectrum is present, one can either limit the processed azimuth bandwidth (as done originally) or apply a squint correction prior to azimuth compression. This correction, with an accurate estimate of the Doppler centroid, f_{DC}, shifts an aliased spectrum back to zero Doppler. The correction applied to range compressed data is given by the linear, range-dependent filter [6]

$$H(x, r') = \exp\left(j2\pi f_{DC}(r')x\right). \tag{4.1}$$

For an entire image to be continuous, all the subimages must be processed with the same squint. If the squint is large, the data may require secondary range compression [6]. After making adjustments for a varying Doppler centroid, the next step in the improvement of the YINSAR motion compensation algorithm is to employ higher-order motion compensation.

4.4 Higher-Order MOCO

As mentioned in Section 3.1, large platform path deviations in SAR imaging create range varying phase error. One solution is to use a higher-order motion

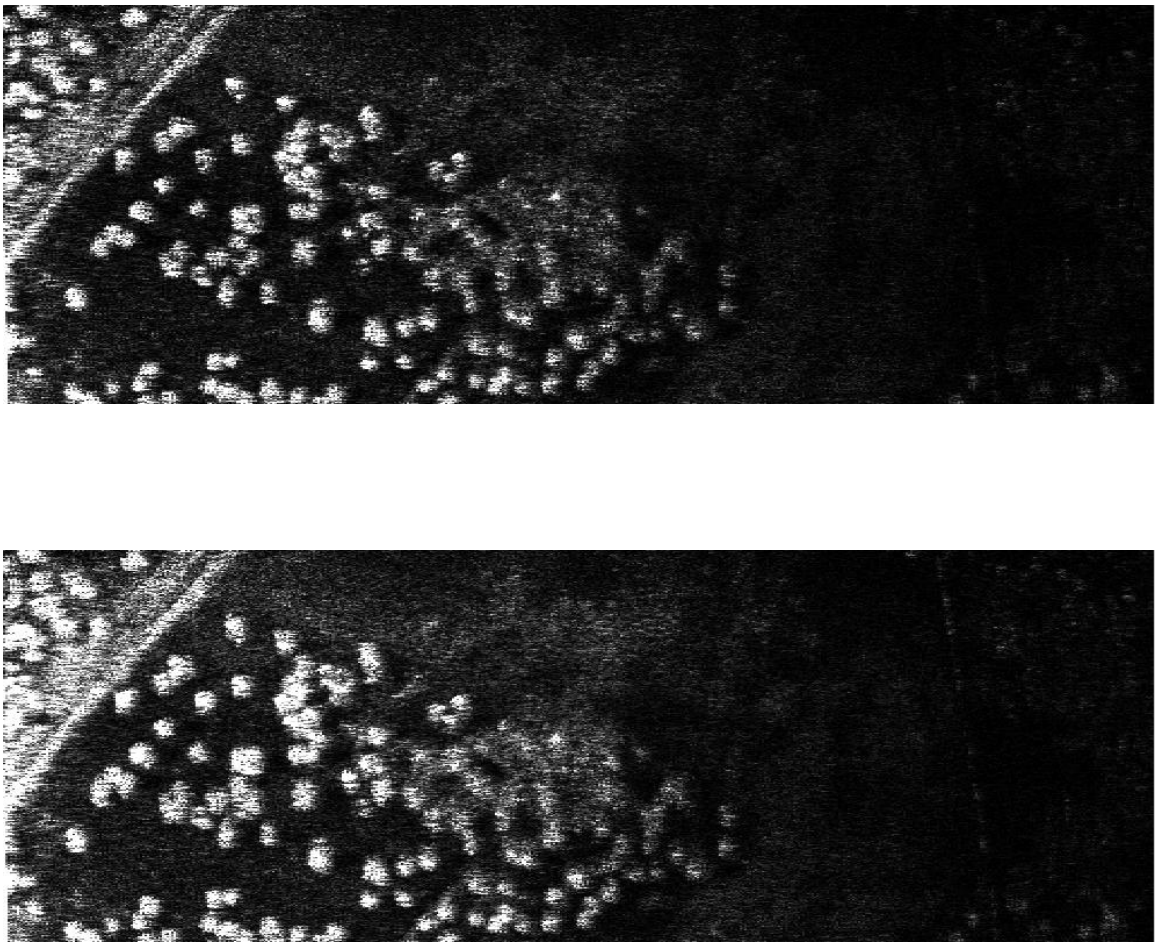

Figure 4.3: Azimuth resolution in improved more azimuth bandwidth is employed. Flight R, pass 1124, top: motion compensated with decreased azimuth bandwidth. Bottom: motion compensated with increased azimuth bandwidth

compensation algorithm. Of the higher-order motion compensation algorithms described in Sections 3.4.2 and 3.4.3, the first choice is the higher-order narrowbeam compensation which applies a second-order correction. This algorithm applies first-order (or bulk) corrections and assumes that any residual motion error is not affected by range migration correction (i.e., the bulk-compensated system is approximately narrowbeam). Using data from pass 2209 of flight U over the Slumgullion slide, the higher-order correction outlined in Section 3.4.2 was employed with the results shown in Fig. 4.4.

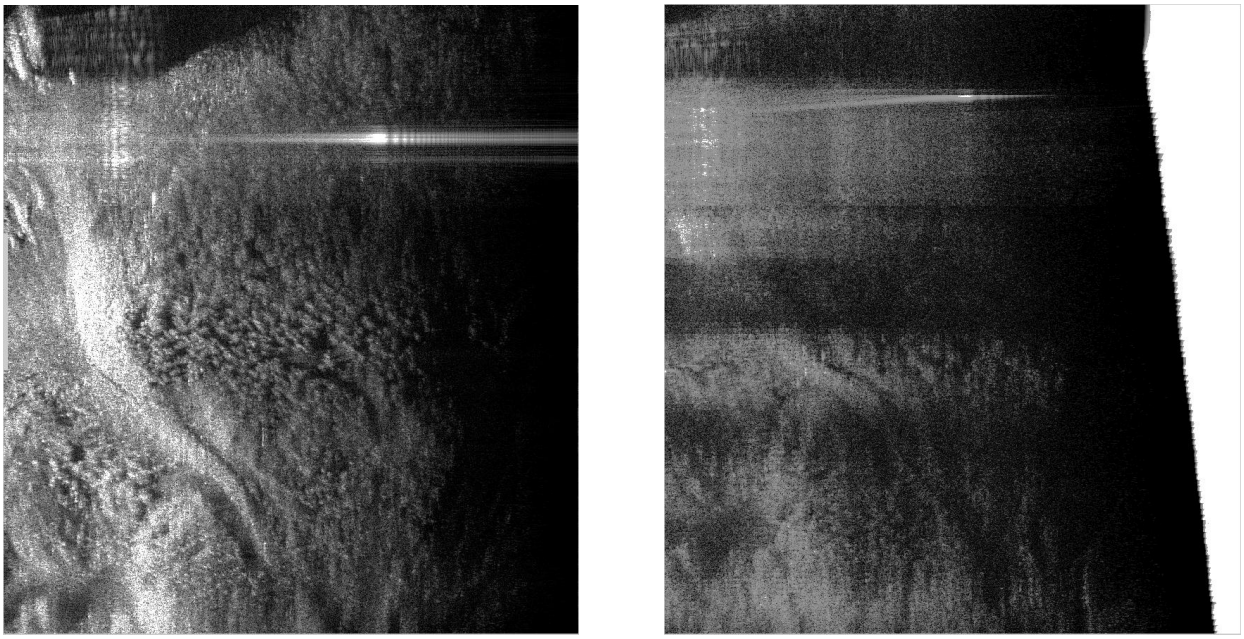

(a) (b)

Figure 4.4: Flight U, pass 2209 over the Slumgullion slide. (a) No motion compensation applied. (b) Higher-order motion compensation applied using a single reference track. Note how higher-order MOCO has degraded image quality due to the large first-order correction created by the large platform deviations.

The most noticable issue with Fig. 4.4 is that higher-order MOCO has not enhanced image quality. This is primarily due to the magnitude first-order corrections which can eliminate interesting parts of the image. Also, if the ideal track is greatly changing over the synthetic aperture, then the azimuth shifting caused by the large

phase corrections causes breaks in the image at azimuth overlap points and produce image distortions (Fig. 4.4). If higher-order motion compensation does not produce desired results, a second option is to segment the ideal track.

4.5 Track Segmentation

The YINSAR motion compensation algorithm creates a single, linear (straight-line) reference track for an entire flight using a linear least squares fit. This approach works acceptably on short flights with low amounts of motion (e.g., passes over Wolfcreek, UT) where the $\delta r(x, r')$ measurements remain small enough that a narrowbeam motion compensation is sufficient (Fig. 4.5).

However, in flights with longer collection times (e.g., Slumgullion slide passes), applying a single, straight-line track to the entire flight track leads to large values of $\delta r(x, r')$ (Fig. 4.6). The results of these large deviations are an increase in range-varying phase error. Applying a narrowbeam correction to these data with large path deviations results in large range bin resampling and distorted images. It is for these types of collections that a segmented reference track may be the best option.

To maintain small deviations for the entire flight, an ideal track is created for each SAR subimage, ameliorating the need for a higher-order correction. The problem associated with segmenting the track is the possibility of image discontinuities. There are two ways that a discontinuity is introduced into an image. First, they occur during the range resampling step if the $\delta r(x, r')$ at the joining points of each subimage differ. The discontinuities become noticeable in the images and interferograms when the differences of $\delta r(x, r')$ between segments become large. Second, discontinuities can occur when the the ideal track segment changes greatly from one segment to the next. This can happen if there is significant high frequency motion. With sufficient overlap between reference tracks is used, image discontinuities are minimized (e.g. Fig. 4.8).

4.6 YINSAR Interferometry

The final area of improvement for YINSAR is motion compensation analysis for a dual channel, bistatic, interferometric radar. As discussed in [5], the model for

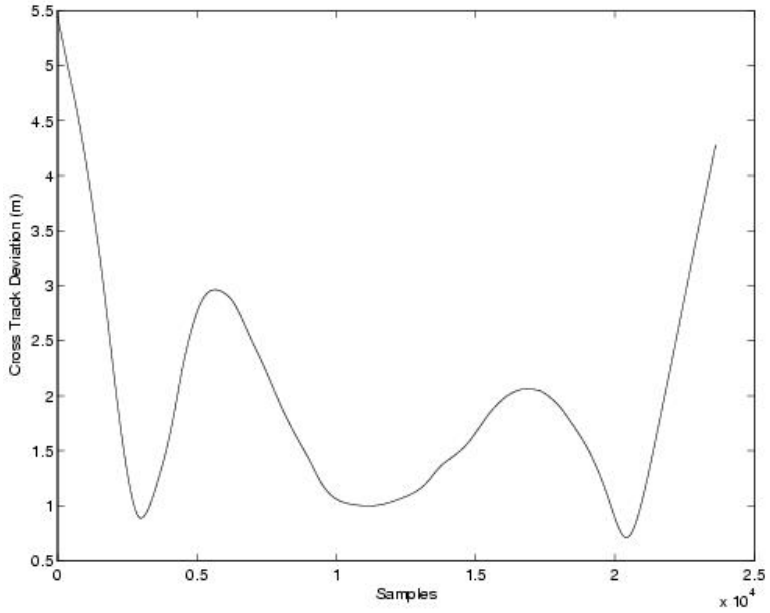

Figure 4.5: Platform deviation from a single,straight-line reference track for pass 1124 of flight R.

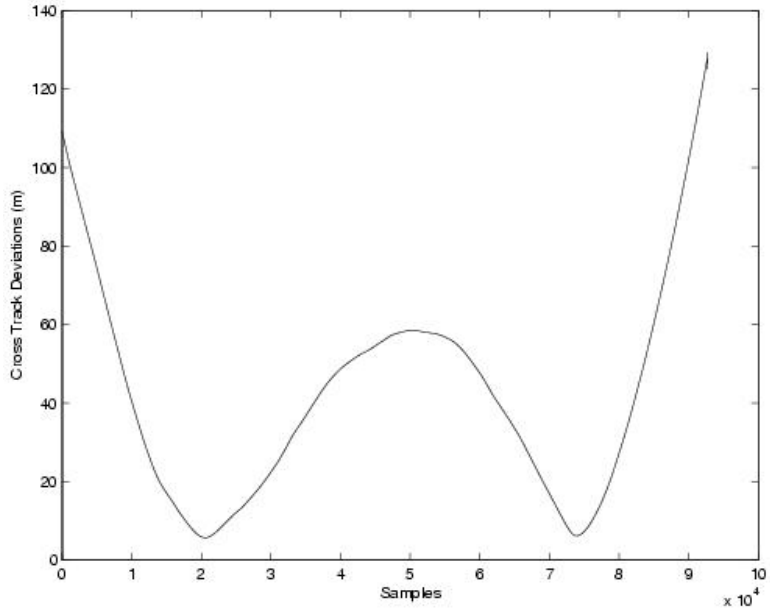

Figure 4.6: Platform deviation from a single, straight-line reference track for pass 2209 of flight U.

Figure 4.7: Flight U, pass 2209 over the Slumgullion slide with no motion compensation applied.

Figure 4.8: Flight U, pass 2209 over the Slumgullion slide with Narrowbeam motion compensation applied using a segmented ideal track.

most interferometric systems includes one bistatic channel and the other monostatic. This model yields an exact height estimate of a target utilizing the fact that the transmit and receive paths for the monostatic channel are the same. In this section the same analysis is extended to YINSAR, which has two bistatic channels. The same narrowbeam motion compensation assumptions apply, which are that motion compensation only consists of a phase correction [5].

4.6.1 Single Reference Track

The assumption for the interferometric measurement model in Section 3.6.1 is that the transmit and return ranges are the same for the monostatic channel, independent of the radar look angle. However, in the case of a bistatic channel, the transmit and receive paths can differ depending on the baseline between transmit and receive antennas or upon the radar look angle. Using the bistatic geometry of Fig. 4.9(a), the applied and ideal motion compensation phase corrections of each channel to a single reference track are given as

$$\begin{aligned}
\phi_A(applied) &= -\frac{2\pi}{\lambda}((r_{To} - r_{to}) + (r_{To} - r_{ao})) && (4.2)\\
\phi_B(applied) &= -\frac{2\pi}{\lambda}((r_{To} - r_{to}) + (r_{To} - r_{bo})) && (4.3)\\
\phi_A(ideal) &= -\frac{2\pi}{\lambda}((r_{Th} - r_{th}) + (r_{Th} - r_{ah})) && (4.4)\\
\phi_B(ideal) &= -\frac{2\pi}{\lambda}((r_{Th} - r_{th}) + (r_{Th} - r_{bh})) && (4.5)
\end{aligned}$$

where r_{To}, r_{ao}, r_{bo}, and r_{to} are the ranges from the reference track, channel A, channel B, and the transmit antenna to the reference height, respectively. Also, r_{Th}, r_{ah}, r_{bh}, and r_{th} are the ranges from the reference track, channel A, channel B, and the transmit antenna to the actual target, respectively.

The resulting single reference track differential phase is given by

$$\begin{aligned}
\Phi_S &= \phi_A(applied) - \phi_A(ideal) - \phi_B(applied) + \phi_B(ideal)\\
&= -\frac{2\pi}{\lambda}((r_{ao} - r_{ah}) + (r_{bo} - r_{bh})). && (4.6)
\end{aligned}$$

In the model of Section 3.6.1, the assumption is that the path from channel A to the actual target is the same as the path to the flat earth estimated target. While not

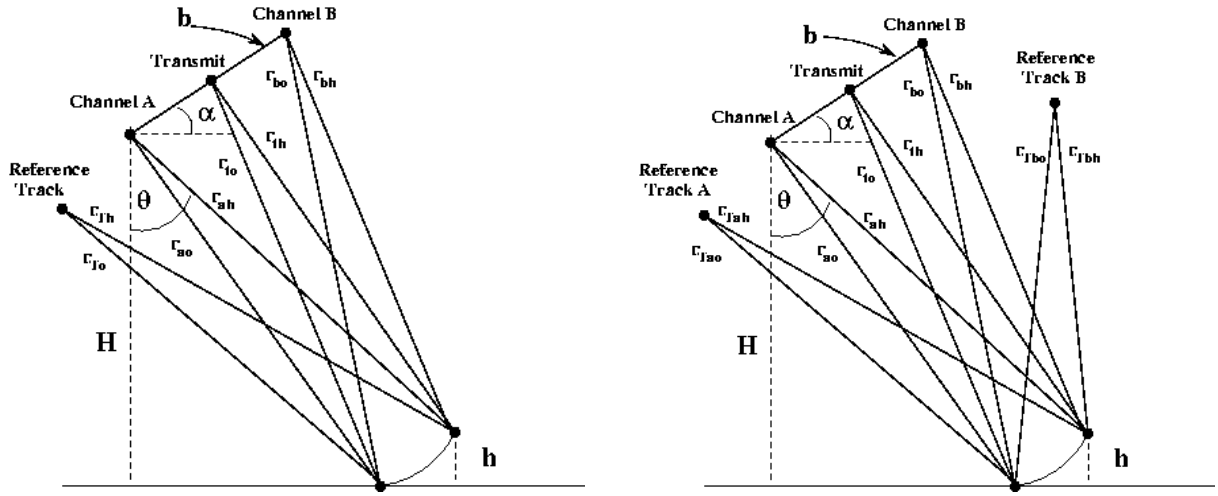

Figure 4.9: (a) Single and (b) double track geometries for a bistatic model.

necessarily true in this case, in this development for convenience we make the same assumption which yields the single track differential phase as

$$\Phi_S = \frac{2\pi}{\lambda}(r_{bo} - r_{bh}). \tag{4.7}$$

So, using the same assumptions as those in the case of a monostatic radar, a height estimate can be found exactly as it was in Section 3.6.1. The look angle to a target is derived using the values computed from motion compensation, r_{ao} and r_{bo} as

$$\theta = \sin^{-1}\left(\frac{\left(\frac{\lambda}{2\pi}\Phi_S + r_{bo}\right)^2 - b^2 - r_{ao}^2}{2br_{ao}}\right) - \alpha \tag{4.8}$$

with the height estimate found as

$$h = H - r_{ao}\cos(\theta). \tag{4.9}$$

4.6.2 Double Reference Track

As in Section 3.6.2, the main benefit of compensating each channel to its own ideal track is to minimize any range migrating phase error. Although the YINSAR has slightly different geometry, the same approach is taken as in Section 3.6.2 with similar results. The resulting differential phase added to the phase difference between

ideal tracks, $\frac{2\pi}{\lambda}(r_{Tah} - r_{Tbh})$, is given as

$$\Phi_S = -\frac{2\pi}{\lambda}((r_{Tao} - r_{Tbo}) + (r_{bo} - r_{bh})). \tag{4.10}$$

As the results in [5], this differential phase does not have the flat earth removed and is sensitive to reference track segmentation. This geometry does not have an exact solution, but can be approximated using a range bin estimate as done in the previous section. The only advantage to using a double track is the feature of minimizing the range migrating phase error.

4.6.3 Application to YINSAR

For YINSAR, the single track motion compensation method is used because of its narrow azimuth beamwidth and limited range migration. The motion compensation consisted of not only the phase correction described in the previous section but also of a range bin resampling. The resampling not only helps correct the two images, but also coregisters them. The resulting interferograms created from the two images are unwrapped using a L_p norm algorithm as specified in [22].

The wrapped and unwrapped interferograms of flight 1124 over Wolf Creek are shown in Figs. 4.10, 4.11, 4.12, and 4.13. A height map created using the estimation of Eqs. (4.8)-(4.9) is shown in Fig. 4.14.

4.7 Summary

In investigating how to improve the motion compensation algorithm for YINSAR, the main areas of improvement were considerations for Doppler centroid, applying higher-order motion compensation, reference track segmentation, and motion compensation considerations for interferometry.

Monitoring changes in Doppler centroid of a SAR image is important to know when the azimuth spectrum aliases. When an azimuth spectrum is aliased, one can limit the processed azimuth bandwidth or apply a squint correction. By limiting the processed Doppler bandwidth, there is a loss of azimuth resolution yet image artifacts

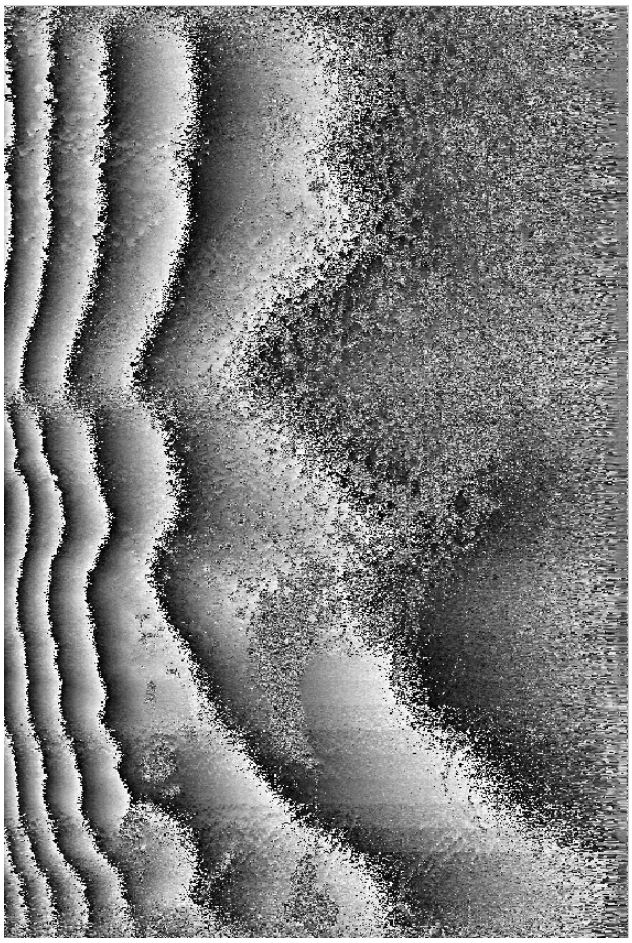

Figure 4.10: A phase wrapped, non-motion compoensated interferogram from pass 1124 over Wolf Creek, UT.

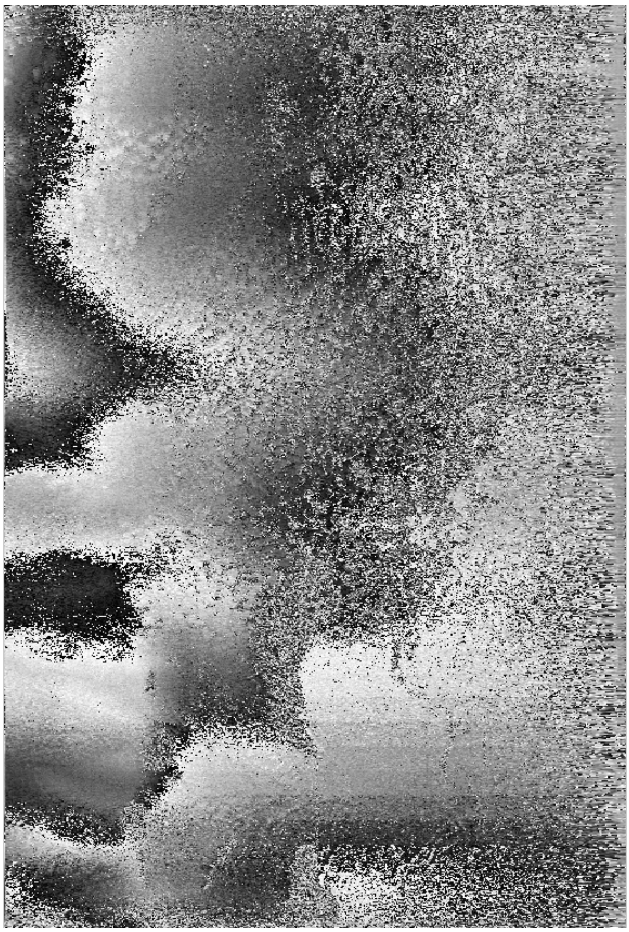

Figure 4.11: A phase wrapped motion compensated interferogram from pass 1124 over Wolf Creek, UT. Note that by compensating both channels to a single track, the a flat earth differential phase is removed – i.e. there are less phase fringes.

Figure 4.12: An average-filtered version of the wrapped, motion-compensated interferotram from pass 1124.

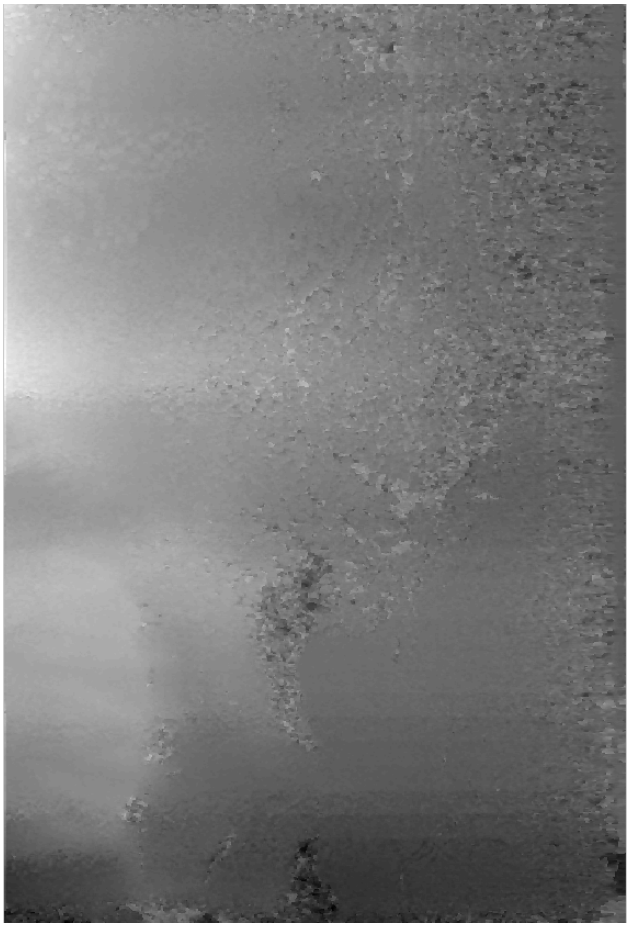

Figure 4.13: The phase unwrapped, motion-compensated interferogram from pass 1124.

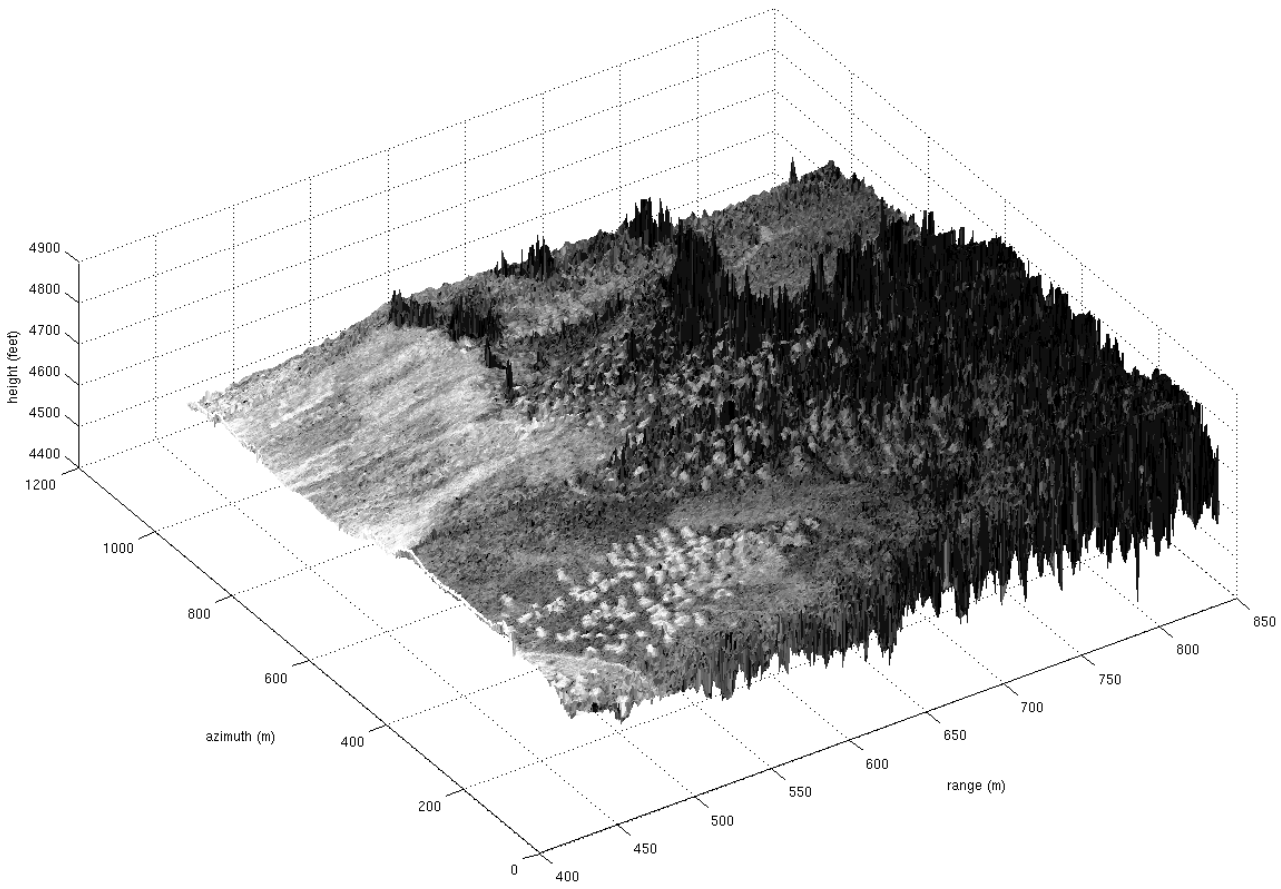

Figure 4.14: Height map of pass 1124 over Wolf Creek, UT. The SAR image has been superimposed onto the height map.

caused from the aliasing are left out. Using a constant squint, a range dependent linear filter can be applied to the data to shift the azimuth spectra back to zero Doppler.

While higher-order motion compensation algorithms appear theoretically attractive to alleviate large deviations in YINSAR, the application of such algorithms does not enhance the imagery and at times introduce error into the images. What proves more successful is the segmentation of the straight-line reference track into multiple straight-line, reference tracks. This approach allows the use of the original narrowbeam motion compensation algorithm, and improved YINSAR imagery.

When considering interferometry, the bistatic nature of YINSAR implies a slightly different model than those of conventional models [5]. However, the modified model produces the virtually the same results and allows for a height estimate using the motion compensation parameters. In considering interferometric motion compensation for YINSAR, a single track approach is used because of its insensitivity to a segmented reference track.

Chapter 5

YINSAR Operation

Although mathematical theory is fundamental to BYU's synthetic aperture radar, YINSAR, its operation and practical usage is also important. This chapter summarizes the practical contributions I have made to the YINSAR program: the implementation, testing and evaluation of other SAR processing algorithms, the verification the translation of the first-order Matlab motion compensation software into C, maintenance of YINSAR hardware, and planning and execution of YINSAR flights to collect data.

5.1 SAR Algorithms

One facet of the YINSAR research I have investigated is the use of other SAR processing algorithms to see if they enable more efficient, improved motion compensation.

SAR processing for YINSAR uses a Range-Doppler algorithm developed by Doug Thompson [25]. One of the shortcomings of this algorithm is the limited azimuth bandwidth required to eliminate the need for any range migration correction. As part of my research, I investigated and implemented the Wavenumber Domain and Chirp Scaling SAR processing algorithms to evaluate other motion compensation methods. As described in the background section, these algorithms differ from the Range-Doppler algorithm in that they better compensate for range migration.

5.1.1 Wavenumber Domain Processor

The Wavenumber Domain algorithm perfectly compensates for range migration but requires computationally intensive two-dimensional interpolations [14]. In the algorithm, the range-compressed data is first converted into the two-dimensional frequency domain using a two-dimensional Fourier transform (see Fig. 5.1) and the ideal matched filter for the center of the image is applied by multiplication in the frequency domain. The effect of this matched filter is to focus the SAR image around the center range, leaving the nearby ranges somewhat focused (Fig. 5.2). The next step is to perform the Stolt interpolation using the expressions in Chapter 2 which focuses the other ranges which are away from the center of the image. The final step is an inverse Fourier transform on the data to produce the image.

A visual comparison can be made between the Wavenumber Domain and Range-Doppler algorithms in Figs. 5.3 and 5.4. As can be seen in the figures, the two algorithms produce virtually the same output with a few differences. First, the Wavenumber domain processor tends to focus a little better and yield improved image contrast. However, more undesirable image artifacts are produced in the Wavenumber Domain processed image than the Range-Doppler processor. Unfortunately, the motion compensation implemented upon the data in the two-dimensional frequency domain is not any more efficient that the implementation in the spatial domain as is done in the Range Doppler algorithm.

Although the Wavenumber Domain processor produced crisp, accurate imagery, the long computation time made it an undesirable choice of algorithm to use for YINSAR.

5.1.2 Chirp Scaling Processor

The next SAR processing algorithm I investigated is the Chirp Scaling algorithm. This algorithm adjusts the phase centers of the received chirps in order to remove the need for interpolation [17] (which is required in both the Range-Doppler and Wavenumber Domain algorithms). The algorithm begins with an azimuth Fourier transform and the application of a "chirp scaling" multiplier. Next, a range Fourier

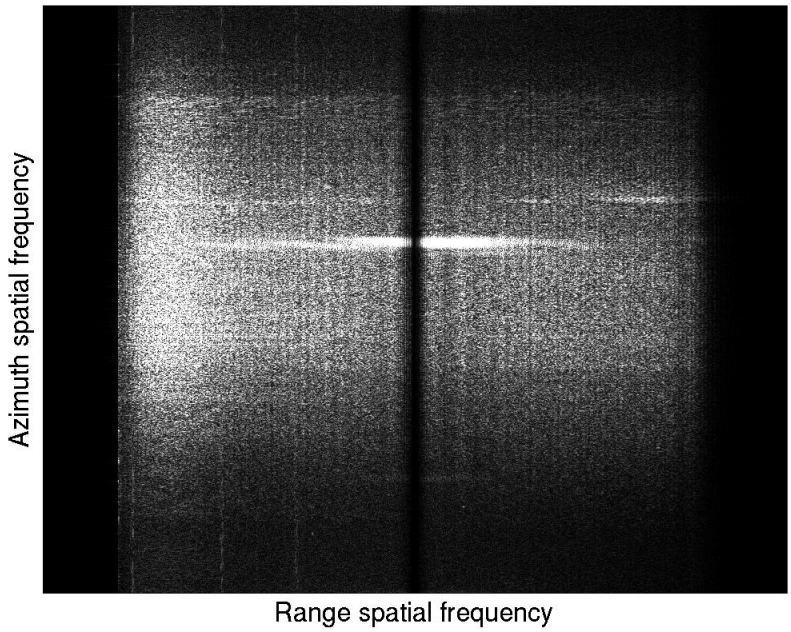

Figure 5.1: Two-dimensional spectrum of range-compressed data. An intermediate step for the Wavenumber Domain processor.

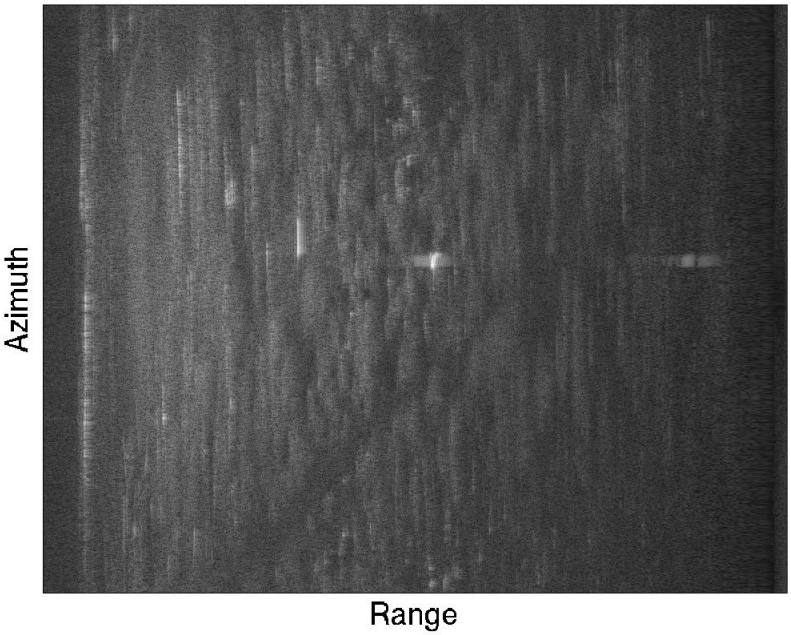

Figure 5.2: Image after the matched filter for the center range is applied. Note how only the center of the image is focused.

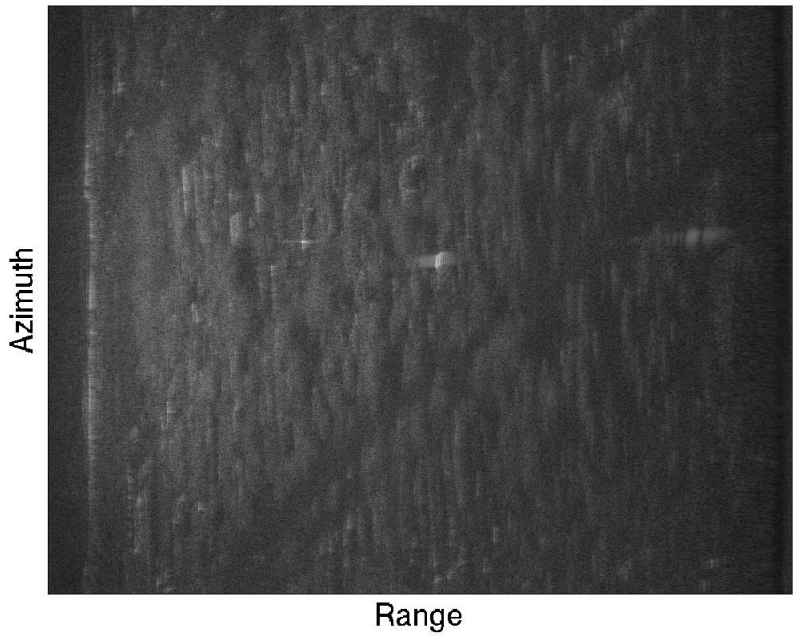

Figure 5.3: Sample image focused using the Wavenumber Domain processor. Note the improved image contrast, but also more undesired artifacts as compared to same image focused with the Range-Doppler algorithm (Fig. 5.4).

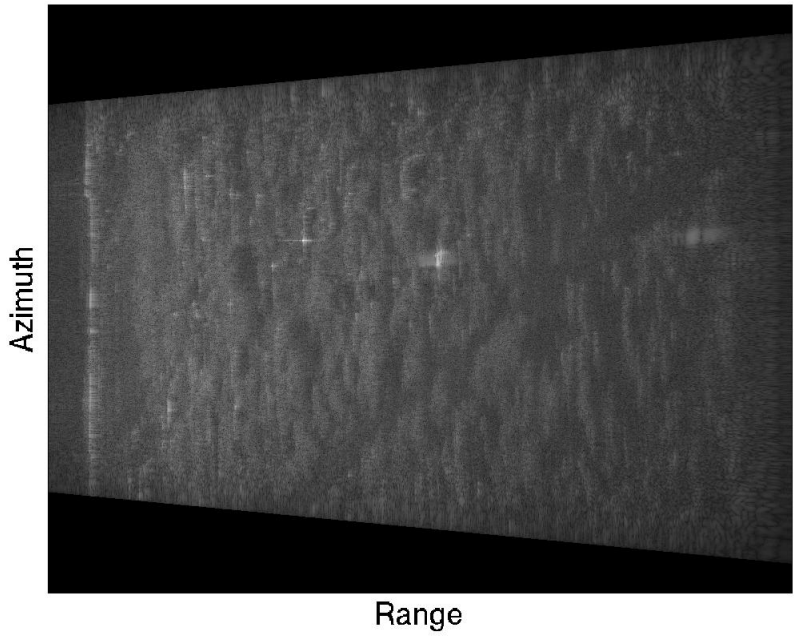

Figure 5.4: The same raw data of Fig. 5.3 is used, but the image is focused using the Range-Doppler processor. The dark edges are artifacts of the processor.

transform is followed by a bulk range migration correction and range compression. The final steps are a range inverse Fourier transform, the azimuth compression and an inverse azimuth Fourier transform.

As seen in Figs. 5.5 and 5.6, the Chirp Scaling algorithm does not focus the image as well as the Range Doppler algorithm. While both use the same azimuth matched filters, the Chirp Scaling algorithm does its range compression at a different step than the Range Doppler. In this implementation, the range compression is not as effective as in the Range-Doppler algorithm and this results in low image SNR. Further, it makes the undesired artifacts more apparent in the image. Although no interpolation is required, the motion compensation requirements remain the same and no improvements to motion compensation are made in the implementation of this algorithm.

While this algorithm tended to process faster than either the Wavenumber Domain or Range-Doppler algorithms, the less effective range compression and the fact that it did not simplify motion compensation made it an undesirable choice as a SAR processing algorithm for YINSAR.

5.2 Motion Compensation

The original YINSAR motion compensation algorithm was written in Matlab by Richard Lundgreen in 1999. In 2001 I validated the algorithm and code and later converted this algorithm to C in 2002 to improve computational time. The C code performs the same operations and functions as the Matlab counterpart aside from a couple of changes. The first difference is between the functions used to convert the GPS latitude/longitude data to UTM. The function written by Lundgreen in Matlab produces inaccurate UTM coordinates, which in some instances are as much as a kilometer off the correct position. The C code is corrected by using the latitude/longitude to UTM conversion function provided in the Jeeps software package [36]. This open source software provides better UTM positions than the previous function. The second difference is the method of removing accelerometer bias. The original code does a direct correction of the INU position data to the GPS position, when in reality

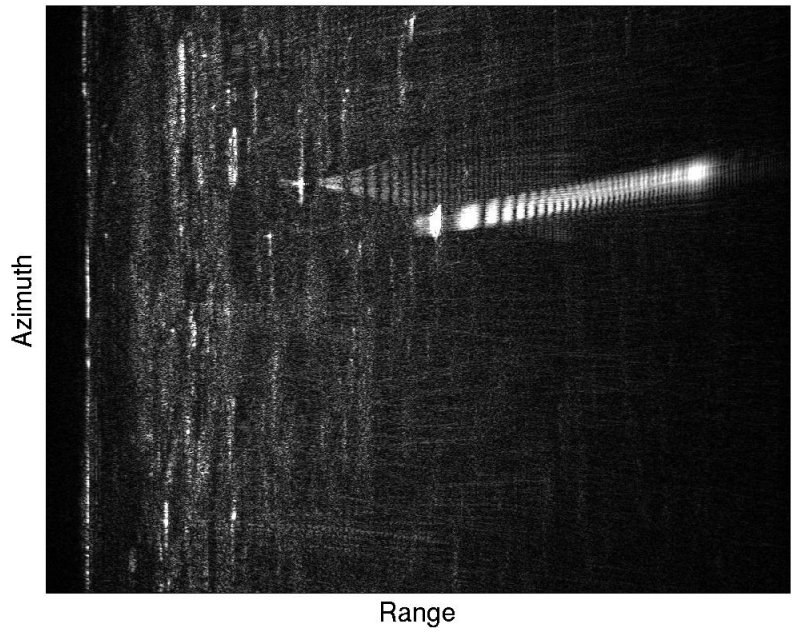

Figure 5.5: Image focused with Chirp Scaling. Note the lowered image SNR due to poor range compression which leads to brighter undesired artifacts.

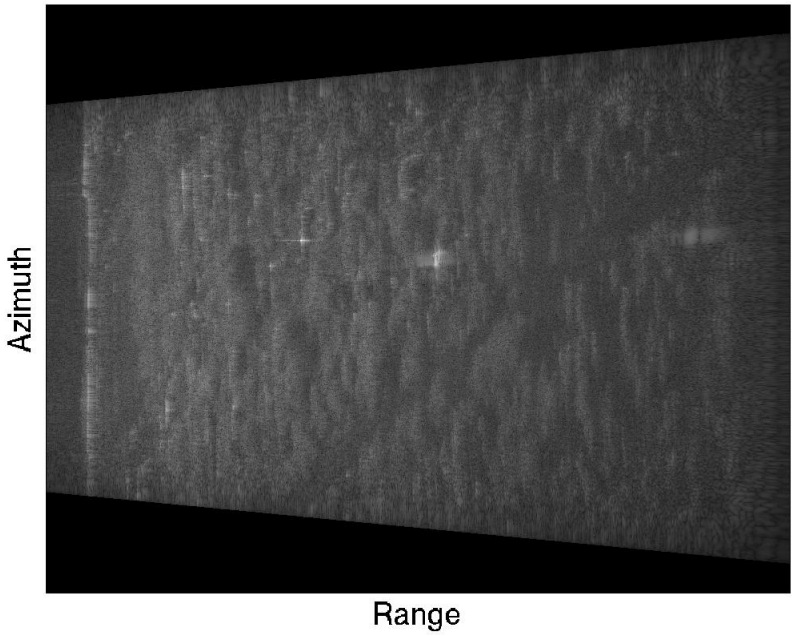

Figure 5.6: Image focused using the Range-Doppler processor. This image is repeated from Fig. 5.4.

a simple parametric, quadratic model is better [37]. The C code implements this quadratic model with a linear least squared error fit.

5.3 YINSAR Maintenance

YINSAR was originally assembled in 1995 by Doug Thompson. Since that time, various upgrades and maintenance operations have been performed. One of the important upgrades I did was the installment of the new differential GPS that uses a satellite-based differential GPS correction called the SATLOC. I installed the hardware receiver into the YINSAR motion box and developed software to interpret the recorded data.

Another hardware issue I addressed is the overheating A/D cards. During many summer data collections the A/D cards in the radar would fail to collect or miss samples due to high temperatures. The problem was corrected by installing various computer cooling fans which helped to improve air circulation in the YINSAR computer box and decrease the chances of overheating.

An unresolved issue is the data storage method. The YINSAR system design contains large IDE hard drives for the collection of large SAR data sets. These storage devices functioned exceptionally well for ground tests, but proved to be very unreliable during actual flights. Through many flights, I diagnosed and discovered the problem to be caused by the vibrations of the aircraft. A solution to this problem is to replace the hard drives with solid state IDE hard drives. This has been left for future work.

5.4 YINSAR Flights

YINSAR has been flown in many areas such as Utah (Logan, Provo, and Wolf Creek) and Colorado (Slumgullion Slide). In most cases, the flight path chosen by the pilot is flat (i.e. at a constant altitude); however in some collections (such as those over the Slumgullion slide), the flight path must be chosen to follow the topography. For instance, for the Slugullion slide flights, this requires descending passes. This tilted flight path complicates processing and requires the processing to be adapted

to handle the slanted path. I modified Doug's Range-Doppler processing and motion compensation to handle this case.

The planning and logistics for a flight represent a significant effort. I planned eight flights and operated the instrument on four of them. A primary responsibility of the radar operator is to estimate the range gate of a flight before collection. It is important that the range gate is set to a correct value and is typically estimated using a rough estimate of the radar above the ground. If the range gate is set too low, much of the image is blank. On the other hand, if the it is set too high, then the final image SNR is too low. Future plans include a method to estimate the range gate for a flight automatically.

After the data from the flights are collected, an archive of the data is created on 9mm and DLT tapes and both stored in the BYU ECEn storage vault. I have created an extensive inventory of all the SAR images from all the collections by YINSAR up until January of 2003. The inventory consists of the images processed with YINSAR Range-Doppler code, the motion compensated images (if available), and a basic plot of the GPS motion data for the flight. Imagery of the various flights are archived on the BYU MERS web page.

5.5 Summary

While the theory of synthetic aperture radar has an important place in the development of YINSAR, so do many of the practical details. Some important contributions to YINSAR has been the implementation of various SAR processing algorithms, the translation of the Matlab motion compensation code into C, the maintenance of YINSAR hardware, and planning YINSAR flights.

Chapter 6

Conclusion

Synthetic aperture radar (SAR) imaging is a useful tool in many applications. Since SAR data processing typically assumes a straight-line flight path, motion compensation is often required to improve imagery. The motion compensation algorithms appropriate to a SAR processor depend upon the radar imaging system. SAR systems with a narrow azimuth beamwidth and that experience small amounts of flight motion can use first-order or narrowbeam motion corrections, while systems that have a large azimuth beamwidth require more complex, widebeam corrections.

Although sufficient for short flights with small motion, the YINSAR narrow beam motion compensation algorithm developed by Lundgreen fails for long flights or with flights that have large deviations. These cases must be corrected by a higher-order motion compensation algorithm or by using a segmented ideal track.

Unfortunately, the higher-order motion compensation proves to be either too computationally costly or eliminates interesting parts of the image due to resampling with a large range error. A segmented ideal track procedure, where the ideal track is locally fit to each data segment, minimizes deviations from the ideal track and allows the use of a narrowbeam motion compensation algorithm to improve final images.

When dealing with motion compensation in interferometry, it becomes a question of whether the two channels are compensated to a single ideal track or whether each track should be compensated to its own reference track. While perhaps more susceptible to range varying phase error, the compensation of the channels to a single track is better of the two methods because of its insensitivity to an ideal track segmentation. Of the two methods, compensating to a single track is used for YINSAR

because of its narrow azimuth beamwidth and use of segmented ideal track on longer flights.

6.1 Contributions

The contributions made through this research are:

- A matlab to C translation of the motion compensation algorithm developed by Lundgreen.
- Improved understanding of the effects of motion on synthetic aperture radar and higher-order motion compensation.
- Analysis of the effects of Doppler centroid on YINSAR and correction methods.
- Research into the effects of motion compensation on a bistatic, interferometric SAR system.
- YINSAR data collection and maintenance.
- Research into the use of a segmented ideal track in YINSAR.

6.2 Future Work

Suggested future work in the area of SAR motion compensation for YINSAR include:

- The design and implementation of a real-time motion compensation system for YINSAR.
- Improving the estimation of platform motion by using the raw data and the RDM and roll estimation techniques found in [32] and [38].
- Investigate techniques to improve YINSAR interferogram correlation using techniques such as Spectral Diversity [39]
- Using improved motion compensation and interferometry, investigate differential interferometry.

- Create improved SAR processing by implementing the wavenumber domain, and chirp scaling algorithms in a lower level programming language, such as C.
- Apply the described motion compensation methods to continuous-wave (FM-CW) SAR.

Bibliography

[1] R.B. Lundgreen, "Method of motion compensation of YINSAR data", Master's thesis, Brigham Young University, 2001.

[2] C.V. Jakowatz, D.E. Wahl, P.H. Eichel, D.C. Ghiglia, and P.A. Thompson, *Spotlight-Mode Synthetic Aperture Radar: A Signal Processing Approach*, Kluwer Academic Publishers, New York, NY, 1996.

[3] USGS, "USGS Landslide Hazards Webpage", http://landslides.usgs.gov, November 2001.

[4] C. Elachi, *Spaceborne Radar Remote Sensing: Applications and Techniques*, IEEE, New York, NY, 1988.

[5] D.R. Stevens, I.G. Cumming, and A.L. Gray, "Options for airborne interferometric SAR motion compensation", *IEEE Transactions on Geoscience and Remote Sensing*, vol. 33, pp. 409–419, March 1995.

[6] J.C. Curlander and R.N. McDonough, *Synthetic Aperture Radar: Systems and Signal Processing*, John Wiley and Sons, Inc., New York, NY, 1991.

[7] B.R. Mahafza, *Radar Systems Analysis and Design Using MATLAB*, Chapman and Hall CRC, Baton Raton, FL, 2000.

[8] R. Balmer, "A comparison of range-Doppler and wavenumber domain SAR focusing algorithms", *IEEE Transactions on Geoscience and Remote Sensing*, vol. 30, pp. 706–713, July 1992.

[9] M. Soumekh, *Fourier Array Imaging*, Prentice Hall, Englewood Cliffs, NJ, 1994.

[10] M. Soumekh, *Synthetic Aperture Radar Signal Processing with MATLAB Algorithms*, John Wiley and Sons, Inc., New York, NY, 1999.

[11] M.Y. Jin and C. Wu, "A SAR correlation algorithm which accommodates large range migration", *IEEE Transactions on Geoscience and Remote Sensing*, vol. 22, November 1984.

[12] J.M. Horrell and M.R. Inggs, "Low frequency range-Doppler SAR processing without secondary range compression", *IEEE Communications and Signal Processing Symposium*, vol. 7-8, pp. 109–114, Sept 1998.

[13] F.H. Wong and I.G. Cumming, "Error sensitivities of a secondary range compression algorithm for processing squinted satellite SAR data", *IEEE Geoscience and Remote Sensing Symposium*, vol. 4, pp. 2584–2587, July 1989.

[14] C. Cafforio, C. Prati, and E. Rocca, "SAR data focusing using seismic migration techniques", *IEEE Transactions on Aerospace and Electronic Systems*, vol. 27, pp. 194–207, March 1991.

[15] H. Choi and D.C. Munson, "On the optimality and exactness of wavenumber-domain SAR data processing", *IEEE International Conference of Image Processing*, vol. 1, pp. 456–460, November 1994.

[16] R.K. Raney and P.W. Vachon, "A phase preserving SAR processor", *IEEE Geoscience and Remote Sensing Symposium*, pp. 2588–2591, 1989.

[17] R.K. Raney, H. Runge, R. Bamler, I.G. Cumming, and F.H. Wong, "Precision SAR processing using chirp scaling", *IEEE Transactions on Geoscience and Remote Sensing*, vol. 32, pp. 786–799, July 1994.

[18] A. Papoulis, *Systems and Transforms with Applications in Optics*, McGraw-Hill, New York, NY, 1968.

[19] D.W. Hawkins and P.T. Gough, "An accelerated chirps scaling algorithm for synthetic aperture imaging", *IEEE Geoscience and Remote Sensing Symposium*, vol. 1, pp. 471–473, August 1997.

[20] G. Franschetti and R. Lanari, *Synthetic Aperture Radar Processing*, CRC Press, FL, 1999.

[21] R. Hanssen and R. Bamler, "Evaluation of interpolation kernels for SAR interferometry", *IEEE Transactions on Geoscience and Remote Sensing*, vol. 37, pp. 318–321, January 1999.

[22] D.C. Ghiglia and M.D. Pritt, *Two-Dimensional Phase Unwrapping: Theory, Algorithms, and Software*, John Wiley and Sons, Inc., New York, NY, 1998.

[23] S.N. Madsen, H.A. Zebker, and J. Martin, "Topographic mapping using radar interferometry: Processing techniques", *IEEE Transactions on Geoscience and Remote Sensing*, vol. 31, pp. 246–256, January 1993.

[24] A. Reigber and R. Scheiber, "Airborne differential sar interferometry: first results at L-band", *IEEE Transactions on Geoscience and Remote Sensing*, vol. 41, pp. 1516–1520, June 2003.

[25] D.G. Thompson, *Innovative Radar Interferometry*, PhD thesis, Brigham Young University, 2001.

[26] G. Fornaro, "Trajectory deviations in airborne SAR: Analysis and compensation", *IEEE Transactions on Aerospace and Electronic Systems*, vol. 35, pp. 997–1009, July 1999.

[27] J.C. Kirk, "Motion compensation for synthetic aperture radar", *IEEE Transactions on Aerospace and Electronic Systems*, vol. 3, pp. 338–348, May 1975.

[28] E.W. Weisstein, "Jacobi-Anger Expansion", From MathWorld–A Wolfram Web Resource, 1999, http://mathworld.wolfram.com/Jacobi-AngerExpansion.html.

[29] C. Prati and F. Rocca, "Focusing SAR data with time-varying Doppler centroid", *IEEE Transactions on Geoscience and Remote Sensing*, vol. 30, pp. 550–559, May 1992.

[30] S.N. Madsen, "Estimating the Doppler centroid of SAR data", *IEEE Transactions on Geoscience and Remote Sensing*, vol. 30, pp. 550–559, May 1992.

[31] R. Bamler, "Doppler frequency estimation and the cramér-rao bound", *IEEE Transactions on Geoscience and Remote Sensing*, vol. 29, pp. 385–390, May 1991.

[32] J.R. Moreira, "A new method of aircraft motion error extraction from radar raw data for real time motion compensation", *IEEE Transactions on Geoscience and Remote Sensing*, vol. 28, pp. 620–626, July 1990.

[33] A. Moreira and Y. Huang, "Airborne SAR processing of highly squinted data using a chirp scaling approach with integrated motion compensation", *IEEE Transactions on Geoscience and Remote Sensing*, vol. 34, pp. 1123–1136, Sept 1996.

[34] S.N. Madsen, "Motion compensation for ultra wide band SAR", *IEEE Geoscience and Remote Sensing Symposium*, vol. 3, pp. 1436–1438, July 2001.

[35] D.R. Stevens, I.G. Cummings, M.R. Ito, and A.L. Gray, "Airborne interferometric SAR: Terrain induced phase errors", *IEEE Geoscience and Remote Sensing Symposium*, vol. 3, pp. 977–979, August 1993.

[36] A. Bleasby, "JEEPS Software Package", July 2000, ftp://ftp.hgmp.mrc.ac.uk/pub/ajb/jeeps/.

[37] S. Buckreuss, "Motion compensation for airborne SAR based on inertial data, RDM, and GPS", *IEEE Geoscience and Remote Sensing Symposium*, vol. 4, pp. 1971–1973, August 1994.

[38] W. Goblirsch, "Motion errors in airborne SAR interferometry", *IEEE Geoscience and Remote Sensing Symposium*, vol. 5, pp. 2668–2670, July 1998.

[39] R. Scheiber and A. Moreira, "Coregistration of interferometric SAR images using spectral diversity", *IEEE Transactions on Geoscience and Remote Sensing*, vol. 38, pp. 2179–2191, September 2000.